The intriguing role of *Phaeocystis spp.* in the ocean ecosystem and biogeochemical cycles

by Sina Müller
Mat. No.: 820544

Master thesis
Institute of Biochemistry and Biology
at
University of Potsdam
in cooperation with
Alfred-Wegener-Institute

supervised by
Judith Hauck, Detlef Groth, Laurent Oziel, Miriam Seifert and Christoph Völker

Date: December 16, 2024

Acknowledgment

I would like to express my gratitude to Prof. Dr. Judith Hauck from the Alfred-Wegener-Institute for the possibility to investigate on the exciting research project of this thesis and the great support. Furthermore, I would like to especially thank Laurent Oziel and Miriam Seifert for the accompany, guidance and shared knowledge throughout the project, Christoph Völker for the support and the MarESys group for the lovely experience to be part of their group.
Additionally, I extend my appreciation to Detlef Groth for the support and guidance, and the University of Potsdam for the great Master course 'Bioinformatics'.
Lastly, thanks to everyone who played a role, directly or indirectly, in helping me achieve this milestone.

Contents

List of Tables

List of Figures

Abbreviations

3D three-dimensional.

AO Arctic Ocean.

AWI Alfred-Wegener-Institute.

BCP Biological Carbon Pump.

C Carbon.

CbPM Carbon-based Productivity Model.

CDOM Colored Dissolved Organic Matter.

Chl-a Chlorophyll-a.

CMIP6 Coupled Model Intercomparison Project Phase 6.

CO_2 Carbon dioxide.

DFe Dissolved Iron.

DIC Dissolved Inorganic Carbon.

DOC Dissolved Organic Carbon.

ESM Earth System Model.

FESIM2 Finite-Element Sea Ice Model, version 2.

FESOM2.1 Finite Element Sea Ice-Ocean Model, version 2.1.

HCO_3^- Bicarbonate.

IPCC United Nations Intergovernmental Panel on Climate Change.

MAREDAT MARine Ecosystem DATa dataset.

MLD Mixed Layer Depth.

N Nitrogen.

NPP Net Primary Production.

NSIDC National Snow and Ice Data Center.

OC-CCI Ocean Colour Climate Change Initiative.

PAR Photosynthetically Active Radiation.

PIC Particulate Inorganic Carbon.

POC Particulate Organic Carbon.

PP Primary Production.

pPFT phyto-Plankton Functional Type.

r Pearson correlation coefficient.

REcoM3 Regulated Ecosystem Model, version 3.

RMSE root mean standard error.

RYF Repeated Year Forcing.

SD Standard Deviation.

SMS Sources Minus Sinks.

SO Southern Ocean.

SPM Suspended particles.

VGPM Vertically Generalized Production Model.

WOA World Atlas Ocean.

zPFT zoo-Plankton Functional Type.

°C degrees Celsius.

Abstract

With climate change, the Arctic Ocean is warming twice as fast as the global ocean. This is causing a cascade of changes, from sea-ice melting over shifts in phytoplankton communities to changes in the biological carbon pump. Ocean biogeochemistry models can be used to better understand those changes and feedbacks. However, projections for the Arctic Ocean have higher uncertainties, pointing towards an underconstrained representation of the Arctic Ocean in models that are still missing important processes and parameters. Therefore, this study aims to introduce another phytoplankton group into the ocean biogeochemistry model FESOM2-REcoM, the so far enigmatic but important group of polar haptophyte species *Phaeocystis spp.* This group is observed to become more prominent in the Arctic Ocean while increasingly affecting the biological carbon pump. A representation of polar *Phaeocystis spp.* in FESOM2-REcoM will allow the simulation of shifts in the Arctic phytoplankton community and concomitant changes in the ecological and biogeochemical cycles as they are observed in field studies.

In this study, I successfully implemented polar *Phaeocystis spp.* into the biogeochemical model REcoM3 and used an established tuning strategy. The knowledge gained from this tuning strategy about the role of parameters can help in future implementations to directly focus on impactful parameters related to the need of the new study. Furthermore, the impact of climate change on the Arctic Ocean in the past five decades could be investigated, which supported findings from several observational studies with regard to physical (i.e. temperature increase and sea-ice melt) and biological changes (i.e. changes in phytoplankton communities). An important observation in this study is the shift in phytoplankton communities from diatoms to increasingly more small phytoplankton species and haptophytes, such as coccolithophores and phaeocystis. In addition, I investigated the impact of this shift on carbon export in the Arctic Ocean, with a focus on the role of phaeocystis for the biological carbon pump. This study further supports the hypothesis that *Phaeocystis* is becoming more prominent in the Arctic Ocean and it is likely that in the future it will expand into the central Arctic Ocean. However, the literature does not agree on whether the community shift is causing an uncoupled NPP-export relationship. This study points out the need for further observational and modeling studies to investigate the so-far obscured role of the arctic community shift on the carbon export in future ice-free regions in the Arctic Ocean.

Zusammenfassung

Aufgrund des Klimawandels erwärmt sich der Arktische Ozean, und das doppelt so schnell wie der globale Ozean. Dies verursacht eine Kaskade von Veränderungen, vom Abschmelzen des Meereises, über Verschiebungen in den Phytoplanktongemeinschaften, bis hin zu Veränderungen in der biologischen Kohlenstoffpumpe. Biogeochemische Modelle der Ozeane können dazu beitragen, diese Veränderungen und Rückkopplungen besser zu verstehen und zu untersuchen. Allerdings sind die Projektionen für den Arktischen Ozean mit größeren Unsicherheiten behaftet, was darauf hindeutet, dass die Modelle den Arktischen Ozean nicht ausreichend abbilden, da wichtige Prozesse und Parameter noch nicht berücksichtigt werden. Daher zielt diese Studie darauf ab, eine weitere Phytoplanktongruppe in das Ozean-Biogeochemiemodell FESOM2-REcoM einzuführen, nämlich die bisher rätselhafte, aber wichtige Gruppe der polaren Haptophytenarten (Phaeocystis spp.). Es wird beobachtet, dass sich diese Gruppe im Arktischen Ozean immer weiter ausbreitet und die biologische Kohlenstoffpumpe zunehmend beeinflusst. Eine Darstellung von polaren *Phaeocystis spp.* in FESOM2-REcoM wird Simulationen von Verschiebungen in der arktischen Phytoplanktongemeinschaft und damit einhergehenden Veränderungen in den ökologischen und biogeochemischen Kreisläufen ermöglichen, wie sie in Feldstudien beobachtet werden können.

In dieser Thesis habe ich erfolgreich polares *Phaeocystis spp.* in das biogeochemische Modell REcoM3 implementiert und eine etablierte Abstimmungsstrategie verwendet. Die aus dieser Abstimmungsstrategie gewonnenen Erkenntnisse über die Rolle von Parametern können bei künftigen Implementierungen helfen, sich direkt auf die für die neue Studie relevanten Parameter zu konzentrieren. Darüber hinaus konnten die Auswirkungen des Klimawandels auf den Arktischen Ozean in den letzten fünf Jahrzehnten untersucht werden, was die Ergebnisse mehrerer Beobachtungsstudien in Bezug auf physikalische (d. h. Temperaturanstieg und Meereisschmelze) und biologische Veränderungen (d. h. Veränderungen der Phytoplanktongemeinschaften) unterstützt. Eine wichtige Beobachtung in dieser Studie ist die Verschiebung der Phytoplanktongemeinschaften von Diatomäen hin zu immer mehr kleinen Phytoplanktonarten und Haptophyten, wie Coccolithophoren und Phaeocystis. Darüber hinaus untersuchte ich die Auswirkungen dieser Verschiebung auf den Kohlenstoffexport im Arktischen Ozean, wobei ich mich auf die Rolle von Phaeocystis für die biologische Kohlenstoffpumpe konzentrierte. Diese Studie stützt die Hypothese, dass Phaeocystis im Arktischen Ozean an Bedeutung gewinnt und sich in Zukunft wahrscheinlich bis in den zentralen Arktischen Ozean ausbreiten wird. In der Fachliteratur herrscht jedoch keine Einigkeit darüber, ob die Verlagerung der Lebens-

gemeinschaft eine entkoppelte NPP-Export-Beziehung verursacht. Diese Studie weist auf die Notwendigkeit weiterer Beobachtungs- und Modellierungsstudien hin, um die bisher verborgene Rolle der Verschiebung der arktischen Lebensgemeinschaften auf den Kohlenstoffexport in zukünftigen eisfreien Regionen im Arktischen Ozean zu untersuchen.

1 Introduction

The ocean is responsible for taking up approximately 25 % of anthropogenic carbon dioxide CO_2 emissions and stores over 50 times more carbon than the atmosphere, mainly due to physical effects [18]. However, it is known for the pre-industrial carbon cycle that biological processes in the ocean play a key role, maintaining atmospheric CO_2 levels approximately 200 ppm lower than they would be in a world with a dead ocean [19], notably through the so-called Biological Carbon Pump (BCP) [20]. The BCP is the suite of biological processes that mediate transport of carbon from the surface ocean to depth and stores carbon in the ocean interior, isolating it from exchange with the atmosphere [21] [22] [23] (see **Box 1**). Despite its first order importance for climate, the United Nations Intergovernmental Panel on Climate Change (IPCC) Assessment Report 6 Working Group I report [24] concluded there is low confidence in the magnitude or even the sign of the effect of climate change on the BCP. One reason for that is the poor and under-constrained representation of biological processes in biogeochemical models [25], a component of an Earth System Model (ESM)[1] which provide the projections for the IPCC (ESMs used by the IPCC, also referred to as Coupled Model Intercomparison Project Phase 6 (CMIP6).

The Arctic is the region which is most impacted by climate change [26] with the "Arctic Amplification" i.e. an atmospheric warming at least four times faster than the global average [27], and the "Arctic Ocean Amplification", i.e. an ocean warming at least two times faster than global average [28]. The most visible consequence is the decrease of the sea-ice area by about 50 % during the last four decades [29]. In fact, the Arctic is expected to experience ice free summers in the second half of the 21st century, regardless of our CO2 emission pathways [24]. As temperatures rise to unprecedented levels, a cascade of changes is altering the full atmosphere-sea ice-ocean system with consequences for both Arctic Ocean's ecosystem and biogeochemical cycles. For example, the melting of sea ice leads to an increased light availability which enhances the Net Primary Production (NPP) achieved by phytoplankton (see **Box 2**) almost linearly by 60 % for the last two decades [30].

[1] ESMs are fully coupled models that additionally consist of a land and an atmospheric component enabling the representation of the full carbon cycle. They allow for climate change induced feedbacks between the different components, and the projection in the future with different emission scenarios.

Box 1: The Biological Carbon Pump (BCP) relates to an inter-play of complex processes involving not only biological, but also counter-intuitively chemical and physical processes. The BCP is intrinsically linked with the structure and the composition of the food web and is illustrated by different "export pathways" (image and following caption description (adapted) from Siegel et al. [23]).

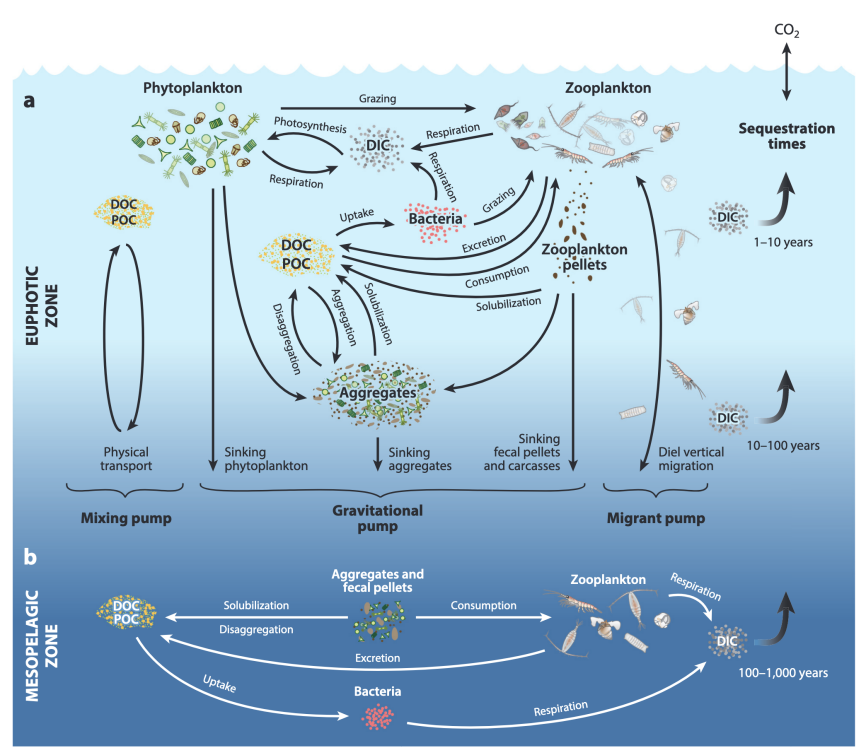

(a) The euphotic-zone food web and the many ecological and biogeochemical processes regulating its relationship with the gravitational, migrant, and mixing pumps that transport organic carbon to depth. The gravitational pump can be summarized as the flux of organic matter to depth by gravity, which is the main contributor to the Carbon (C-) export [31]. In the mixing pump export to depth is driven by physical transport [21] while in the migrant pump by vertically migrating organisms [32].
(b) Beneath the euphotic zone, organic carbon is remineralized back to Dissolved Inorganic Carbon (DIC) via food-web processes in the mesopelagic zone. The depths to which that organic carbon is transported set the timescale of its sequestration. Abbreviations: Dissolved Organic Carbon (DOC), POC.

Box 2 - Phytoplankton: The name comes from the Greek words $\phi\upsilon\tau\acute{o}\nu$ (phyton), meaning 'plant', and $\pi\lambda\alpha\gamma\kappa\tau\acute{o}\varsigma$ (planktos), meaning 'wanderer' or 'drifter'. Phytoplankton are marine microscopic algae that represent the main oceanic autotrophs. Phytoplankton perform photosynthesis, i.e. they harvest light using pigments such as Chlorophyll-a (Chl-a) and convert inorganic carbon in the form of CO_2 and Bicarbonate (HCO_3^-) into organic carbon compounds such as sugars and biomass. When light and nutrient conditions are optimal, phytoplankton fix more inorganic carbon than what is lost through respiration, thereby producing biomass which eventually leads to the formation of blooms (see for example below a satellite 'true-color' image of a bloom of coccolithophorids in the Barents Sea, which are visible as turquoise colour because of their calcite platelets that reflect light). This production of organic matter (or NPP) is the first step of the BCP and also sustains the entire marine ecosystem, since they represent the first link in the trophic chain.

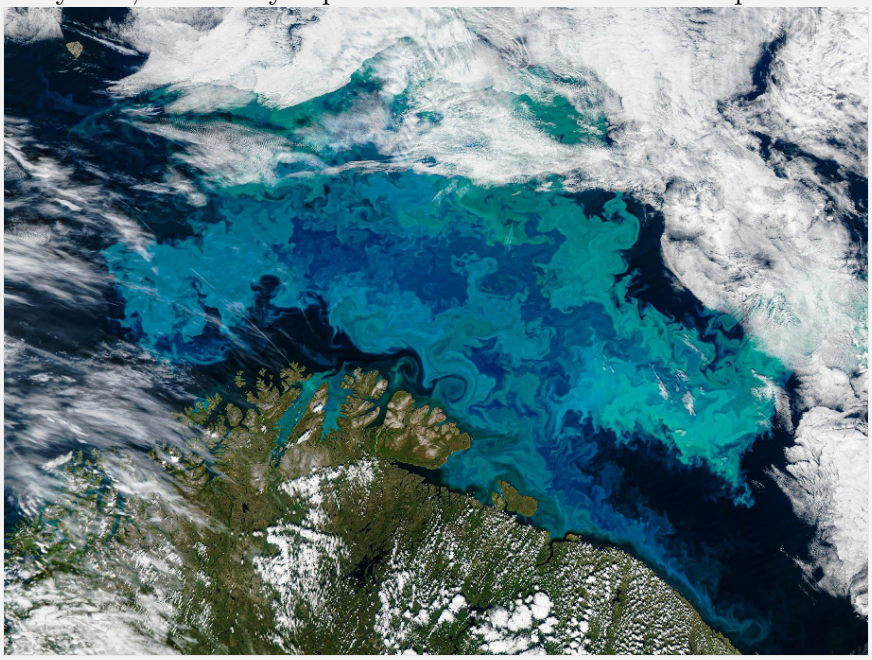

©NASA / OBPG Group

However, the paradigm that increased light availability is the primary cause of higher phytoplankton productivity is changing. Instead of increased photosynthetically active radiation (PAR), increased nutrient input seems to progressively be the main driver of enhanced phytoplankton NPP in the Arctic Ocean (AO) [17]. To sustain this growth, phytoplankton need to take up more and more nutrients to support the increasing biomass in the surface waters. CMIP6 models also recently came to a consensus that NPP in the

AO is expected to continue increasing in the future. However, uncertainties in their projections for the AO are considerably higher than for the global ocean [33], making statements on the future of the Arctic NPP and BCP difficult if not impossible. This large inter-model uncertainty is likely caused by diverse ways of representing physical and biogeochemical processes in the models [33]. Moreover, several processes of the BCP are not or only poorly constrained in models [34]. Without an existing and precise description of these processes, models are unable to reliably represent the BCP and its sensitivity to change, which is a prerequisite for robust projections of future scenarios [34]. Thus, I hypothesize that biogeochemical processes or parameterizations are missed that are crucial for the AO.

Main objective: Among the many missing processes in the 'state-of-the-art' biogeochemical models, the focus of this study will be on the addition of a missing phytoplankton group: the haptophyte *Phaeocystis spp.* (**Box 3**). In particular, I pay attention to *Phaeocystis pouchetii*, one of the rare colony- and bloom-forming species inhabiting the sub-Arctic regions. It has been largely overlooked in biogeochemical models, but I suspect that it has a growing role in both the AO ecosystem and biogeochemical cycles because of the following reasons:

1. The Arctic is typically dominated by large cell diatoms. Diatoms need silicic acids to produce their frustules made of silicate. There is evidence that the one main supply of silicic acid with the poleward transport of Atlantic water is decreasing [35].

2. There is continuously more satellite evidence of poleward intrusions of temperate haptophyte species such as coccolithophorids [36] and *Phaeocystis spp.* [37] into the AO.

3. There is also in situ evidence for a shift in the phytoplankton composition towards more haptophytes [38].

4. Because of the specific properties of the *Phaeocystis* colonies, which are embedded in gelatinous matrices, they can have large implications on both the food web and the BCP if they were to replace other phytoplankton groups such as diatoms [39].

Box 3 - *Phaeocystis spp.* is a (group of) flagellated algae belonging to the haptophyte genus that have a highly variable lifestyle, as they can occur in diverse environmental habitats. Only three species are able to form colonies: *P. pouchetii*, occurring in the sub-arctic regions, the focus of this study, *P. antarctica*, occuring in the Southern Ocean (SO) and *P. globosa*, occurring globally in the temperate regions. Colonies are enveloped in a gelatinous matrix which could protect them from grazing by predators. This mucus, consisting of polysaccharides, may also be responsible for increased carbon export to depth when ballasted with minerals [39]. *P. pouchetii* do not need silicic acid to grow unlike diatoms, and also may be more efficient and flexible at harvesting Nitrogen (N) (the most limiting nutrient in the AO, [40]) from inorganic and organic sources [41].

As part of this thesis, I implemented a new pPFT corresponding to *Phaeocystis pouchetii* (in the AO) and *P. antarctica* (in the SO) into the biogeochemical model that is used and developed at the Alfred-Wegener-Institute (AWI) a German polar institute and an ESM provider). The biogeochemical model is the REcoM3 [42] which is coupled to the general circulation and sea-ice model, the Finite Element Sea Ice-Ocean Model, version 2.1 (FESOM2.1) [43]. To achieve this, I will use, wherever possible, model parameters derived from observations collected in laboratories (temperature response, photosynthetic parameters). Then, an extensive manual tuning of the three-dimensional (3D) model is conducted in order to arrive at reasonable large-scale spatio-temporal distribution and magnitude of core variables (NPP, biomass, Chl-a, gravitational pump, upper-ocean fields of nutrients, etc). Finally, the model is used to conduct a hindcast simulation (1970-2023) to investigate phytoplankton community shifts and emerging hotspots of carbon export in the AO.

2 Materials and Methods

2.1 Model Description

In this study, the biogeochemical model FESOM2-REcoM3 is used. The model is written in Fortran version 2021.6.0 using the Intel Fortran Compiler version 2022.1.0.
For the analysis of model output, post-processing scripts were used, such as the adjusted 'Global Assessment'-Script from the MarESys-Group AWI'. This as well as further analysis scripts, written in Python, version 3.10.13 were used [44]. Additionally, the R software, version 4.4.1 was used [45]. All Softwares and Packages are summarized in Appendix .4)
FESOM2 is a sea-ice model, which solves for sea ice concentration, thickness and drift. It is coupled to the biogeochemistry and ecosystem model, which calculates the cycling of nutrients and carbon via physics and biological components such as phyto- and zooplankton. A more detailed description can be found below.

I start from an improved version of the standard REcoM3 model [42], coupled to the ocean general circulation model FESOM2.1 [43]. The standard version of REcoM represents only two pPFTs: Diatoms and other "small phytoplankton". The model version used in this thesis additionally incorporates a third pPFT representing the calcareous coccolithophorids [3], which, with the addition of "phaeocystis", raises the total number of pPFTs to four. Also, the version I use has three zooplankton, zoo-Plankton Functional Type (zPFT) size classes (macro-, meso- and microzooplankton) rather than two in the standard version (macro- and mesozooplankton). Both versions use two detritus size classes (slow and fast sinking detritus, [46]. Finally, our version uses a parametrization for the ballasting of detrital particles by minerals [47] [48] that was absent in the standard version.

As I use it in its ocean-only configuration, the ocean is forced with atmospheric reanalysis from the JRA55-do dataset, a surface-atmospheric dataset using satellite and other atmospheric validation products, ranging from 1958 to present and having a spatial resolution of 55 km and a temporal resolution of 3h [49]. Land-ocean fluxes such as freshwaters and biogeochemical fluxes from rivers are also prescribed.

The coupled model uses a 3D mesh – longitude, latitude and depth. Longitudes and latitudes have a nominal resolution of one degree as background. The mesh has a higher resolution in the equatorial regions, due

to higher dynamics because of increased upwelling of nutrient-rich waters leading to increased biological activity [50]. Also, the AO is represented using a higher resolution. The water column is represented with 48 unevenly spaced vertical layers. The layer thickness ranges from five meters at the surface (again, higher resolution due to higher dynamics) to 250 meters in the deep ocean [51]. The model calculates a model step every 15 minutes, however, the output can be averaged in consideration to the user's needs. In this study, the output is written as the monthly average.

The FESOM2.1 model incorporates two tracers, salt and temperature, and handles 33 passive biogeochemical tracers from REcoM3 to track their advection and diffusion. FESOM2.1 calculates the sea-ice components like sea-ice concentration, ice and snow thickness as well as the ice-drift-velocity using the Finite-Element Sea Ice Model, version 2 (FESIM2) [52], which is incorporated into FESOM2.1.

The ocean-biogeochemistry is simulated by REcoM3. It calculates Sources Minus Sinks (SMS), driven by biological interactions or biogeochemical feedback processes [42]. It represents the cycling of carbon, oxygen and nutrients with varying intracellular stoichiometry of phyto- and zooplankton, as well as variability in the stoichiometric composition of detritus. The pPFTs represented in the model are responsible for the marine Primary Production (PP). Their individual internal stoichiometry is defined as followed: Diatoms – C:N:Chl:Si (silicification), coccolithophores – C:N:Chl:CaCO3 (calcification) [3], small phytoplankton – C:N:Chl [42]. The internal stoichiometry of the newly implemented pPFT phaeocystis will be defined like the internal stoichiometry of the small phytoplankton pPFT (i.e, C:N:Chl), as it does not form body structures out of silicate or calcium carbonate [39]. Thereby three biogeochemical tracers (PhaeoC, PhaeoN and PhaeoChl) are added to REcoM3 resulting in a total of 36 tracers.
Furthermore, zooplankton feed on phytoplankton, other zooplankton, and detritus [46] [48]. The grazing preference of microzooplankton is defined to be highest for small phytoplankton, while meso- and macrozooplankton are defined to prefer larger prey such as diatoms, phaeocystis and microzooplankton. Macrozooplankton additionally feed on mesozooplankton. Meso- and macrozooplankton produce fast sinking organic matter and thereby largely contribute to the long-term carbon storage [53] [39].

2.2 Technical Background on the Implementation of a new Phytoplankton Group into REcoM3

The growth rate or net photosynthesis rate of a pPFT, μ, is described by a temperature dependency f(T), a light dependency f(PAR), a nutrient de-

pendency f(nut) and a dependency on the carbonate system f(CO_2) minus the respiration rate (Eq. 1). The temperature dependency f(T) describes the maximal achievable growth rate per day at zero light, nutrient, and carbonate system limitations. All functions are pPFT-specific:

$$\mu = (f(T) \cdot f(\text{PAR}) \cdot f(\text{nut}) \cdot f(\text{CO}_2)) - \text{resp. rate} \tag{1}$$

with a respiration rate calculated via a pPFT-specific maintenance respiration constant (resPhy) modified by the uptake limiter factor (limitFacN; listed in Table **1**), the cost of biosynthesis (constant value of 2.33 [mmol C (mmol N)$^{-1}$]; biosynth) as well as the nitrogen assimilation (Nassim; as defined in Eq. 7). In the following, the equation for the calculation of the phaeocystis respiration rate is shown:

$$\text{resp. rate}_{phaeo} = resPhy_{phaeo} \cdot limitFacN \cdot biosynth \cdot Nassim_{phaeo} \tag{2}$$

The Carbon (C)-specific photosynthesis rate is defined as an exponential saturation curve (in equation 3 shown for phaeocystis), representing the rate of carbon fixation of a pPFT. As seen in the photosynthesis-irradiance curve following the model of [2] in Figure **1**, it approaches the pPFT-dependent maximum photosynthetic rate (Pmax) in a logarithmic manner. The initial slope of the PI-curve is representing the light harvesting efficiency (alfa). The higher the value, the higher the efficiency at low PAR. The decay of the saturation curve also depends on a variable intracellular Chl-a to C ratio (Chl:C) of a pPFT and Photosynthetically Active Radiation (PAR) [2]. The photosynthesis rate is also dependent on the carbonate system, hence f(CO_2) is multiplied:

$$P_{phaeo} = \left(Pmax_{phaeo} \cdot 1.0 - \exp\left(-\frac{alfa_{phaeo} \cdot \text{Chl:C}_{phaeo} \cdot \text{PAR}}{Pmax_{phaeo}} \right) \right) \cdot f\left(CO_2(phaeo)\right) \tag{3}$$

The limitation function of CO_2, f(CO_2), is based on a modified Michaelis-Menten function, accounting for the concentrations of bicarbonate and CO_2 as well as pH in the water column (Eq. 4, Fig. **2**) [54] [3]. HCO_3^- and CO_2 are the aqueous concentrations of bicarbonate and CO_2, respectively, and a, b, c, d being pPFT-specific parameter values from fitting the function to experimental data [3]. The final value of f(CO_2) is restricted to 0 and 3 as lower and upper bounds, respectively. For phaeocystis, f(CO_2) parameters of the small phytoplankton group were taken (listed in **1**).

$$f(CO_2) = \left(\frac{\alpha_{phaeo} \cdot HCO_3^-}{\beta_{phaeo} + HCO_3^-} \right) - \exp\left(-c_{phaeo} \cdot CO_{2(aq)}\right) - d_{phaeo} \cdot 10^{-pH} \tag{4}$$

Pmax is dependent on temperature and nutrient limitation (Eq. 5), defined using a rate constant (µmax) multiplied by f(T) and the nutrient limitation f(nut):

$$Pmax_{phaeo} = \mu_{max} \cdot f(T) \cdot f(nut) \tag{5}$$

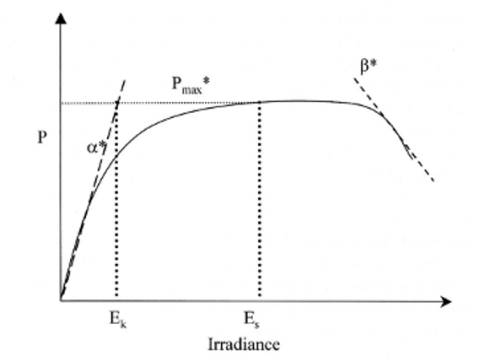

Figure 1: **Photosynthesis-irradiance curve [1], following the model from [2]Geider et al. [2]** Showing biomass production based on irradiance including α – the initial slope, Pmax – the maximum photosynthesis rate and β – the exponential loss term for photodamage at high irradiance. E_k is the saturation index defined as the intersection between α and Pmax; $E_s$is the irradiance at which Pmax is reached for the first time (light saturation). While E_k is an important measure in experimental photophysiology, E_s is a rather arbitrary number as it can barely be determined in the laboratory.

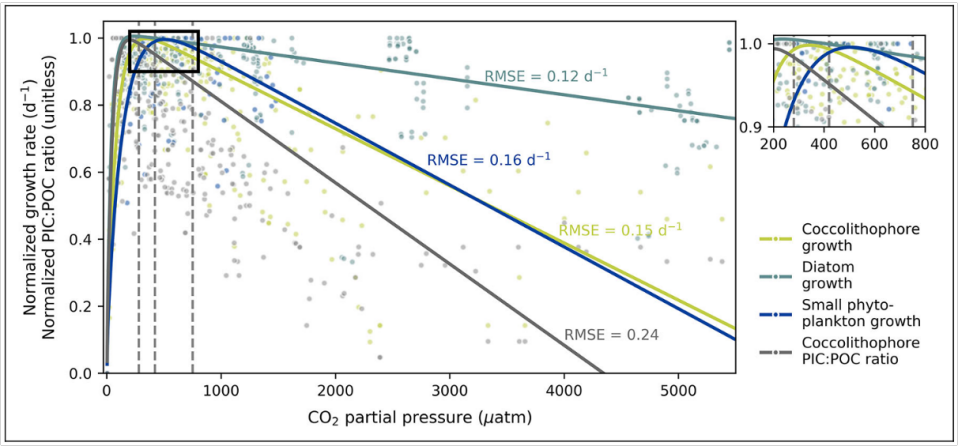

Figure 2: **Growth rates relative to CO_2 partial pressure [µatm] [3].** The represents the pPFT dependency on the carbonate system (Eq. 4), showing growth of coccolithophore (green), diatom (lightblue) and small phytoplankton (dark blue) and coccolithophore PIC:POC ratio for calcification (hence specific for the coccolithophore PFT). For curve fitting, the data was normalized to values between 0 and 1. The fitting of the growth curve of small phytoplankton (dark blue) was also used for the implementation of phaeocystis.

The nutrient function, f(nut), represents the nutrient limitation, con-

straining the growth of pPFT regarding nutrient availability. A value of 1 indicates nutrient-replete conditions (no limitation) whereas a value of 0 means complete limitation. The limitation is given by the most limited nutrient (Eq. 6). By limiting Pmax, the nutrient functions limit the photosynthetic rate of a PFT, hence C uptake, influencing the internal stoichiometry of a PFT:

$$f(nut)_{phaeo} = min\left(limitationDIN, limitationDFe\right) \tag{6}$$

The temperature dependence f(T) of phaeocystis was newly added in collaboration with a PhD student in the group (Hannah Haines, Alfred-Wegener-Institute, Bremerhaven, Germany), as described in chapter: 'Temperature function derivation for phaeocystis' in 'Materials and Methods'-section. In parallel to this study, new temperature functions for diatoms, coccolithophores and small phytoplankton were also used that were derived using a quantile regression method by fitting a curve to observational data by Hannah Haines (Fig. **3**).

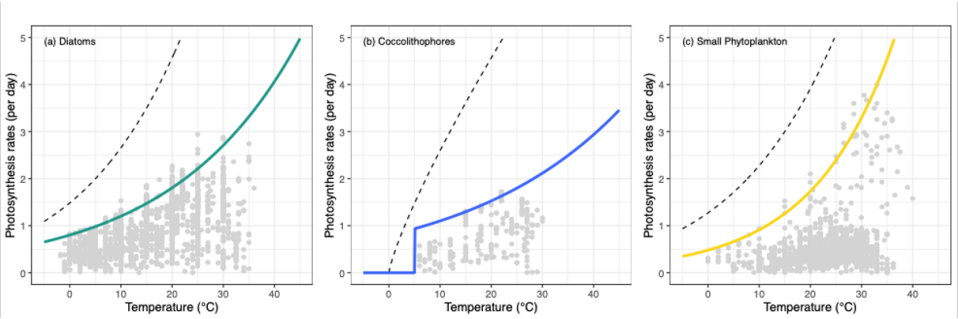

Figure 3: **Temperature functions of pPFTs.** In parallel to this study, new temperature functions were developed for the four pPFTs in REcoM3. For diatoms (a), coccolithophores (b) and small phytoplankton (c) the new temperature functions were derived empirically using quantile regression from the observational data of Anderson et al. [4] (in colors) whereas the old functions were based on the Arrhenius model [5] (in grey) (derivation and figure by Hannah Haines).

The description of variable stoichiometry including nutrient uptake and photoacclimation in REcoM is based on the so-called "Geider model" [2] and modified as described in Gürses et al. [42]. The uptake of nutrients of a pPFT, referred to as DIN assimilation (Nassim), is, amongst other terms, dependent on the Michaelis-Menten kinetics using a half-saturation constant k which is pPFT-specific (Eq. 7). The lower k, the more efficient the nutrient uptake at lower nutrient concentrations. Further parameters are explained in Table **1**.

$$Nassim_{phaeo} = V_{cm} \cdot Pmax_{phaeo} \cdot limitFacN \cdot \frac{DIN}{DIN + k(din)_{phaeo}} \tag{7}$$

REcoM3 does not model internal iron pools within each pPFT and, hence, iron assimilation is not described for any phytoplankton functional type. Iron limitation is computed using the Michaelis-Menten kinetics based on the external pool of Dissolved Iron (DFe) (not shown). The Chl-a synthesis rate of a pPFT is described as a function proportional to DIN assimilation (Nassim), the maximum Chl to N ratio (Chl:Nmax) and the current maximum photosynthesis rate (P), based on PAR, Chl:C and alfa. However, P is constrained to an upper bound of 1 (Eq. 8):

$$\begin{aligned} Syn_{Chl,phaeo} &= Nassim_{phaeo} \cdot \text{Chl:N}_{phaeo} \\ &\cdot min\left(1, \frac{P_{phaeo}}{alfa_{phaeo} \cdot \text{Chl:C}_{phaeo} \cdot PAR}\right) \end{aligned} \tag{8}$$

The C-specific photosynthesis rate (Eq. 3), the nitrogen assimilation (Eq. 6) and the Chl-a synthesis (Eq. 8) describe the sources of the internal stoichiometry of phaeocystis – C:N:Chl. Each component of the internal stoichiometry of each pPFT, but also for zooplankton, is calculated using the SMS function.

The sinks are described by loss of C/N/Chl-a. Sinks for N and C are losses occurring via excretion (lossN, lossC) as dissolved organic nitrogen/carbon, respectively DON/DOC, via aggregation of the pPFT (agg) and grazing by the zooplankton groups (mesozooplankton - G_{Z1}, macrozooplankton - G_{Z2}, microzooplankton - G_{Z3}). An additional sink of C is via respiration. Excretion loss is scaled by the uptake limiter factor (limitFacN) and the internal N/C concentration (PhaeoN/C). The aggregation and respiration is also scaled by PhaeoN/C. The SMS function of N and C can be described as in equation 9 and 10, respectively:

$$\begin{aligned} SMS_{N,phaeo} &= Nassim_{phaeo} \cdot PhaeoC \\ &- lossN_{phaeo} \cdot limitFacN_{phaeo} \cdot PhaeoN \\ &- agg \cdot PhaeoN \\ &- \sum_{j=1}^{3}(G_{Zj,phaeo}) \end{aligned} \tag{9}$$

$$\begin{aligned} SMS_{C,phaeo} &= P_{phaeo} \cdot PhaeoC \\ &- lossC_{phaeo} \cdot limitFacN_{phaeo} \cdot PhaeoC \\ &- agg \cdot PhaeoC \\ &- resp.rate_{phaeo} \cdot PhaeoC \\ &- \sum_{j=1}^{3}(G_{Zj,phaeo}) \end{aligned} \tag{10}$$

The SMS function of Chl-a of phaeocystis is shown in equation 11. The source is described by the Chl-a synthesis function (SynChl, phaeo) and sinks of Chl-a are described by a degradation rate of Chl-a (K0Chl), the aggregation (agg) of the pPFT as well as the grazing of zooplankton (mesozooplankton - G_{Z1}, macrozooplankton - G_{Z2}, microzooplankton - G_{Z3}) on the pPFT:

$$\begin{aligned} SMS_{Chl-a,phaeo} = & \, Syn_{Chl,phaeo} \cdot PhaeoC \\ & - K0Chl_{phaeo} \cdot PhaeoChl \\ & - agg \cdot PhaeoChl \\ & - \sum_{j=1}^{3} (G_{Zj,phaeo} \cdot \text{Chl:N}_{phaeo}) \end{aligned} \tag{11}$$

The degradation rate of Chl-a (K0Chl; Eq. 12) is described via a linear function of light availability (PAR), the pPFT-specific degradation rate constant (degChl) and the intracellular Chl:C ratio (Chl:C). It is allowed to vary between a lower bound of 10 % of degChl, and an upper bound of 0.3 [day^{-1}] derived from Álvarez et al. [55].

$$K0Chl_{phaeo} = degChl_{phaeo} \cdot \text{Chl:C}_{phaeo} \cdot PAR \tag{12}$$

2.3 Temperature Function for phaeocystis

To define the growth rate (μ) of a pPFT, the growth needs to be described in relation to temperature. For single species, temperature dependence of growth follows the thermal reaction norm, an asymmetric curve that describes minimum, maximum, and optimum growth temperatures [56]. In models, pPFTs usually represent numerous species of which each can be described by a single temperature function. The sum of temperature functions of the species within a pPFT can then be described by an exponential function [4]. However, as the pPFT phaeocystis only describes two species (*P. pouchetii* and *P. antarctica*), the resulting temperature function will not be exponential but gaussian-like. Data from different laboratory studies was collected for *P. pouchetii* and *P. antarctica* [6] [7] [8]. Models for temperature functions: symmetrical and asymmetrical Gaussian, Hinchelwood, Eppley-Norberg (models not shown) and Blanchard (shown in Eq. 14), summarized by Grimaud et al. [56], were tested for the potential as temperature functions and fit to the observational data. Laboratory studies usually report growth rates or net photosynthesis rates which already include carbon loss by respiration. As respiration is considered as a separate loss term in REcoM, the laboratory growth rate data had to be corrected to account for respiration, resulting in the gross photosynthesis rate. Therefore, the growth rates were amplified inversely by the averaged respiration factors taken from

López-Sandoval et al. [57] and Bozzato et al. [58] from the observational data (Eq. 13):

$$photosynthesisrate = \frac{growthrate}{1 - resp.average} \tag{13}$$

where resp. average represents the mean respiration factors for each model pPFT (e.g., phaeocystis: 0.15) computed from Bozzato et al. [58].

For fitting the different models to the observational data, the nls.LM function from the minpack.lm (version 1.2-4) in R was used. It combines the Nonlinear Least Squares with the Levenberg-Marquardt algorithm, which finds the best parameters for models using weighted residuals with minimized sum of least squares. The fitted models were then used to derive growth rates for a temperature range between -2 and 16 degrees Celsius (°C), like the one of the observational data, using the 'predict' function from the stats package in R. The plotted predictions were then used to choose the most suitable growth rate function for phaeocystis.

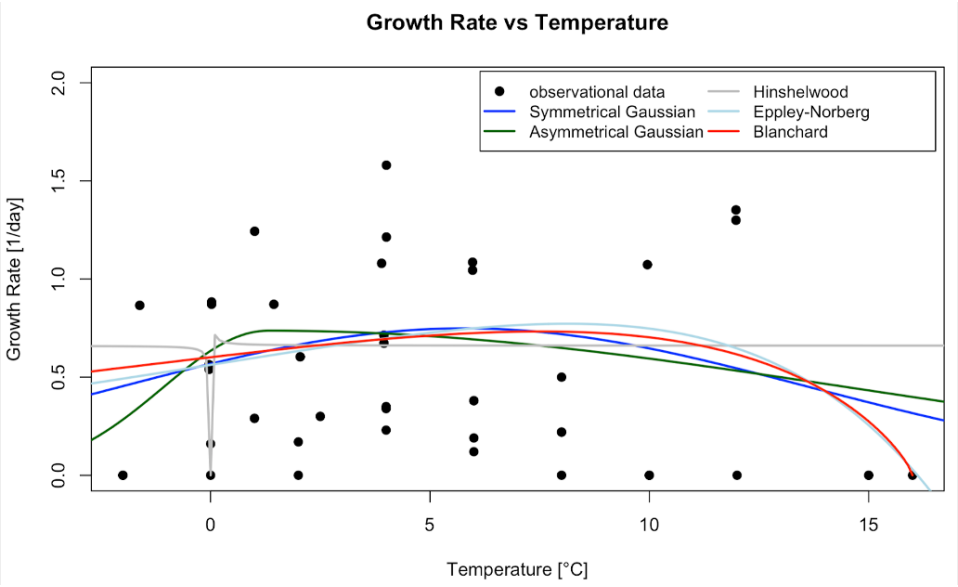

Figure 4: **Tested growth-temperature model functions.** Fit of different models (symmetrical (dark-blue) and asymmetrical (green) Gaussian, Hinshelwood (grey), Eppley-Norberg (light-blue) and Blanchard (red) for temperature functions of phaeocystis to observational data of polar species *P. pouchetii* and *P. antarctica* from Schoemann et al. [6], Wang et al. [7] and Buschmann [8].

As I aim to only implement *P. pouchetii* and *P. antarctica* into REcoM3, with a focus on the Arctic *P. pouchetii*, a growth model limited to a temperature range of 0 - 14 °C as given in the literature [7] is important. As

both Gaussian functions as well as the Hinshelwood function allow growth outside this range they are unsuitable for describing the two polar phaeocystis species. The Eppley-Norberg model allows for negative growth, hence loss, which is also not appropriate to represent phaeocystis.

The Blanchard model describes increasing growth up to 8 °C, followed by an increasing decline, until it reaches zero at 16 °C, not allowing for growth in more temperate waters like the temperate and tropical waters. Therefore, this function is selected to describe the growth rate for phaeocystis in REcoM (Eq. 14; Fig. **4**, red curve) with parameters listed in Table 1. Additionally, growth was defined to cease at temperatures of 0°C and below. The blanchard function (Eq. 14) describes the growth rate (µ) by using a maximum temperature (Tmax), an optimum growth temperature (Topt), an optimum growth rate (µopt) and b. Parameter values for Tmax, Topt, and Tmin were determined by fitting the function to observational data from *P. pouchetii* and *P. antarctica*. Parameters and their values are listed in Table 1:

$$f(T) = \mu_{opt} \cdot \left(\frac{T_{max} - T}{T_{max} - T_{opt}} \right)^{b} \cdot exp(-b \cdot \left(\frac{T_{opt} - T}{T_{max} - T_{otp}} \right) \qquad (14)$$

Table 1: **Relevant parameters in the REcoM3 for phaeocystis.** Main newly integrated parameters for phaeocystis implementation.

Parameter	**Value**	**Unit**	**Description**
T_{max}	16	°C	Blanchard temperature model: maximum temperature
T_{opt}	6.7982	°C	Blanchard temperature model: optimum growth temperature
μ_{opt}	0.6903	[day^{-1}]	Blanchard temperature model: optimum growth rate
b	0.7114	unitless	Blanchard temperature model: dimensionless parameter
$alfa_p$	0.17	[mmol C m^2 (mg Chl W day)$^{-1}$]	Initial slope of PI-curve of phaeocystis
pzPhaeo	0.5	unitless	Grazing preference of mesozooplankton on phaeocystis
pzPhaeo2	1.0	unitless	Grazing preference of macrozooplanktonon phaeocystis
pzPhaeo3	0.25	unitless	Grazing preference of microzooplankton on phaeocystis
$lossN_p$	0.05	[day^{-1}]	Nitrogen loss of phaeocystis; same for all pPFTs

$lossC_p$	0.1	[day^{-1}]	Carbon loss of phaeocystis; same for all pPFTs
$degChl_p$	0.075	[day^{-1}]	Chl-a degradation constant of phaeocystis
$resPhy_p$	0.01	[day^{-1}]	Maintenance respiration rate constant; same for all pPFTs
$Chl{:}Nmax_p$	2.6	[mg Chl mmol N^{-1}]	Maximum Chl-a to N ratio of phaeocystis
$k(din)_p$	0.7	[mmol N m^{-3}]	half-saturation constant of nitrogen uptake of phaeocystis
$k(Fe)_p$	0.09	[µmol Fe m^{-3}]	half-saturation constant of iron uptake of phaeocystis; same as coccolithophores
P_{phaeo}	0.75	[day^{-1}]	C-specific photosynthesis rate of phaeocystis
$Pmax_{phaeo}$	variable	[day^{-1}]	maximum C-specific photosynthetic rate of phaeocystis
$Nassim_{phaeo}$	variable	[mmol N (mmol C $day)^{-1}$]	Nitrogen uptake of phaeocystis
$limitFacN_{phaeo}$	variable	unitless	limiting factor of Nitrogen uptake (if zero, no uptake as intercellular N:C ratio reaches max)
NCuptake $Ratio_p$	0.2	[mmol N mmol C^{-1}]	Maximum uptake ratio of N:C; same for all pPFTs
$NCmax_p$	0.15	[mmol N mmol C^{-1}]	maximum intracellular N to C ratio; reversed Redfield C:N = 6.6
$NCmin_p$	0.04	[mmol N mmol C^{-1}]	minimum intracellular N to C ratio; same for all pPFTs
Vcm_p	0.7	unitless	scaling factor for C-specific N-uptake; same for all pPFTs

Table 2: **Already existent parameters in the REcoM3 changed during tuning.** Changed parameters, already existent in REcoM3, differences to the values of the previous model version are shown in parenthesis.

Parameter	**Value**	**Unit**	**Description**
grazMax3	0.36 (-0.1)	[mmol N m^{-3} day^{-1}]	general grazing factor of microzooplankton
grazMax2	0.25 (+0.15)	[mmol N m^{-3} day^{-1}]	general grazing factor of macrozooplankton

pzCocco3	0.5 (+0.5)	unitless	Grazing preference of microzooplankton on coccolithophores
$degChl_d$	0.2 (+0.05)	[day^{-1}]	Chl-a degradation constant of diatoms
$alfa_n$	0.15 (+0.01)	[mmol C m^2 (mg Chl W $day)^{-1}$]	Initial slope of PI-curve of small phytoplankton
$degChl_n$	0.15 (-0.1)	[day^{-1}]	Chl-a degradation constant small phytoplankton

2.4 Observational Data for Model Evaluation

For the tuning and the model evaluation, observational data of global planktonic biomass was taken from the MARine Ecosystem DATa dataset (MAREDAT) [59]. For the global ocean Chl-a remote-sensing data, the Ocean Colour Climate Change Initiative (OC-CCI) dataset from Sathyendranath et al. [14] was used. For the AO, the Chl-a dataset from Lewis et al. [60] was used in addition to the OC-CCI dataset. Compared to the OC-CCI dataset, Lewis et al. [60] corrects empirically, using observational data, the Chl-a over-estimation in coastal areas due to the influence of terrigenous inputs (i.e. absorption of Colored Dissolved Organic Matter (CDOM) and Suspended particles (SPM).
Global datasets for NPP were taken from the Carbon-based Productivity Model (CbPM) dataset from Westberry et al. [15] and the Vertically Generalized Production Model (VGPM) from Behrenfeld and Falkowski [16]. CbPM derives VGPM from C-biomass and growth rate, while VGPM is a chlorophyll-based algorithm.
Arctic data for NPP comparison was taken from Lewis et al. [60], as well as Globcolor (GlobColour data (http://globcolour.info) used in this study has been developed, validated, and distributed by ACRI-ST, France). Additionally, remote sensing data for Chl-a in the SO was taken from Johnson et al. (2013). The temperature, salinity and nutrient distribution calculated by the model was compared to data from the World Atlas Ocean (WOA) (Garcia et al., 2018). Data for comparing the Mixed Layer Depth (MLD) was taken from Sallée et al. [10] and sea ice trends in September were compared to observational data from the NSIDC [11].

2.5 Tuning Strategy

After a suitable temperature function was found, tuning was conducted according to the following strategy. 20 years spin-up simulations were performed using Repeated Year Forcing (RYF), a single repeating annual cycle of all forcing fields (atmospheric, oceanic and land). For forcing, the year

1961 of the JRA55-do v1.4.0-clim61 dataset [49] was chosen as it is rather neutral regarding atmospheric conditions.

Parameters were first determined according to literature values and used for a base-run. More precisely, alfa of phaeocystis ($alfa_p$), the initial slope of the PI-curve which determines the light harvesting efficiency at low PAR, was initially set to that of small phytoplankton, hence 0.14. Furthermore, the upper-bound of the internal N:C ratio (reversed Redfield-Ratio C:N) of phaeocystis was observed to be close to the Redfield Ratio of 6.6 [61] [62], and therefore set to the reversed standard value of 0.15. Literature upon grazing on phaeocystis is contradictory [39], but it is suspected that grazing of microzooplankton can induce colony formation and, hence, a size misfit between predator and prey [63]. Due to this, I assume in this study that there is limited grazing pressure by microzooplankton, while rather large zooplankton (i.e. meso- and macrozooplankton) have a higher preference for phaeocystis prey. Therefore, the grazing preference on phaeocystis (macrozooplankton – pzPhaeo2, microzooplankton – pzPhaeo3) was initially set to 1.0 and to 0.5 for macro- and microzooplankton, respectively. For loss terms of N and C, the same values as for all other PFTs were chosen (see Table 1). For the degradation rate of Chl-a ($degChl_p$) an initially low value of 0.075 was chosen. For the upper-bound of the intracellular Chl:N ratio of phaeocystis ($Chl{:}Nmax_p$) we follow the modeling study of Nissen and Vogt [64] who chose a parameter value that is 62.5 % of the value of diatoms for *P. antarctica* in their ocean model ROMS-BEC.

According to the result of these model outputs compared to observational data, the parameters were further investigated and tuned to improve the representation of phaeocystis as well as of biogeochemical and biological fields (listed in Table **1** with final values). To argue for or against a better representation, the model output of biomass, NPP, Chl-a and nutrients was compared regionally and globally to respective observational data using the 'Global Assessment'-Script from MarESys (AWI). The script was previously adjusted for the analysis of phaeocystis. In the investigation process, the parameters were changed solely, while leaving any other unchanged. Parameters showing promising enhancements of the model output were later combined to investigate synergistic effects of these. In combination with the tuning of the newly developed temperature functions, investigated by Hannah Haines, a total of 52 "tuning strategy"- runs were performed, in the following referred to as tuning runs. A summary of tuning runs are listed in Table **3**. For simplicity and focus of this work, tuning runs for temperature functions will be neglected.

Table 3: **Summary of tuning strategy using RYF.** Shows the number of the tuning runs (#), their aim as well as its expected outcome (hypothesis) and if this is met or not.

#	**Aim**	**Hypothesis**	**Hypothesis met?**
1	baserun	-	-
2,3,6,7, 10,11,12, 13,24,26 29,35,41	Investigating grazing preferences on different pPFTs	Increasing grazing preferences decreases pPFT biomass, regarding regional overlap between specific zPFT and pPFT	Yes
4,5,8,9, 15,22	Investigating the effect of alfa of the pPFTs	Increase of alfa increases biomass, NPP and Chl-a	Yes
14	Investigating the effect of changed upper bound of N:C ratio (reversed Redfield Ratio)	Increase of N:Cmax constraints pPFT growth more in an N-limited environment (AO)	Yes
16,17	Investigating the effect of half-saturation constants on Phaeocystis (k(din)), k(Fe)	the lower k, the better the uptake at low concentrations; increase decreases biomass under limitation	Yes
23,30	Investigate synergistic effect of changes in $NCmax_p$ and $k(din)_p$	decreasing $NCmax_p$ and $k(din)_p$ increases biomass of phaeocystis in AO	No
27,34, 40,42	Decrease Chl-a concentrations, especially in the AO (degChl, Chl:Nmax)	Increase of degChl decreases Chl-a concentration; Decrease of Chl2Nmax constraints Chl-a concentration more regarding N limitation	Yes
36	adjusting grazing rates of zooplankton ($grazMax_z$)	Increase of grazing rates should increase overall biomass of zooplankton hence will also increase grazing pressure on pPFTs	Yes
43,44,50 51,52	test synergistic effects of changed parameters	-	-

2.6 Transient Simulation

To evaluate the final tuned model and to investigate how phaeocystis behaves under real atmospheric changes over the past 54 years (1970-2023), a transient run using inter-annually varying atmospheric forcing was conducted. With the final tuned version, using parameters listed in Table **1**, a 60 year spin-up run was performed to bring the model in a quasi-equilibrium

using constant RYF with the year 1961 as described above. Thereafter, the last spin-up year was used as a start for a transient simulation which was conducted for the years 1959 to 2024, using atmospheric forcing from JRA55-do v.1.4.0 (1959 to 2019) and v.1.5.0 (2000-2024) [49].

2.7 Model Evaluation

After the implementation of phaeocystis in the model, the model was evaluated. For this, the transient run was used to have a look at the temperature, salinity, MLD, sea-ice and nutrients (DIN and DSi) calculated by the model compared to observational data. Additionally, NPP, Chl-a and biomass of all pPFTs together (total), but also for each pPFT separately were evaluated. A focus was set to the AO and phaeocystis. For the evaluation the adjusted 'Global Assessment'-Script was used, like for the model tuning step (Fig. **10- 15**). For temperature, salinity and nutrients as well as Chl-a and NPP, the Taylor statistics (Standard Deviation (SD), Pearson correlation coefficient (r), root mean standard error (RMSE)) were calculated for the comparison to observational data [65].

Firstly, environmental and physical factors (Fig. **10**) like temperature and salinity were vertically integrated over the upper 100 meters and compared to the WOA dataset [9]. The density threshold for the MLD was set to 0.03 kg m^{-3} as in de Boyer Montégut et al. [66]. Based on this, the MLD was calculated for the months March and September and compared to the dataset from Sallée et al. [10]. Sea-ice extent in AO in September [million km^2] from 1979 to 2019 was compared to the dataset from NSIDC. The global DIN and DSi concentrations were reviewed and also compared to observational data. To do so, upper-ocean (0 - 100 m) DIN/DSi outputs from the transient model run were integrated and the average of the last 10 years were taken (Fig. **14/ 15** A) and compared to the WOA dataset [12]. The differences between model output and observational data were calculated and shown in figure **11**.

The global distribution of biomass in the averaged last eleven years (2013 - 2023) for the four pPFTs is shown in Figure **12**. The vertically and horizontally integrated biomass was used to compare the relative contribution of each pPFT in the phytoplankton community. Furthermore, the biomass of each PFT (including zooplankton) was compared to observational data from the MAREDAT [59].
To assess the distribution of NPP, the model output data was globally compared to VGPM and CbPM observational data. The distribution of Chl-a was compared to OC-CCI data (global) and [13] for the SO (data not shown). Also, the latitudinal distribution of NPP and Chl-a for each of the

four pPFTs as well as the total amount was compared to observational data (shown in Fig. **13**).
Figures **14** and **15** show the distribution of total NPP and Chl-a in the AO, respectively. It compares the model output (1A/2A) to observational data from Lewis et al. [17](1B) as well as the GlobColour (NPP) and the OC-CCI (Chl-a) dataset (2B). In C, the differences are shown. Two different sets of observational data were used for validation because of the bias between the two sets of observational data. During tuning, the aim was to minimize the bias shown in C, while keeping an eye on the other variables (biomass, global Chl-a, NPP and nutrient distribution). Model output was averaged over the same time period as the respective observational data. For the analysis of biomass and NPP model output was vertically integrated, while for Chl-a only the surface concentrations were used.

2.8 Analysis of the Role of phaeocystis using Hindcast Simulations

To analyze the overall changes of phaeocystis and total NPP and carbon export (C-export) flux over time (1970-2023), a timeseries of total NPP (totalNPP), phaeocystis NPP (NPPp) and the C-export flux was plotted (Fig. **16**) for the global ocean as well as for the AO (> 66°N). The C-export flux is the downward flux of organic carbon across a certain depth horizon, typically 100 m. In this study, I plotted the flux for 100 m (global ocean and AO) and for 30 m (AO only). To focus on potential changes in the phytoplankton composition in the AO, and primarily, to investigate if and where phaeocystis is becoming increasingly prevalent in the AO, the absolute linear trend of NPP and Chl-a concentrations for each pPFT and in total was plotted using numpy.polyfit — NumPy v2.1 Manual, n.d (Fig. **17** and **19**). Additionally, a relative trend was calculated by taking the difference between the linear regression's first year and last year value and dividing it by the first year value multiplied by the years and finally multiplied by 100 % (Fig. **18** and **20**). Both, absolute and relative analyses, were performed with a focus on the AO.

3 Results

3.1 Tuning Strategy

During the tuning process, different parameters were investigated and combined with others that showed promising changes. For example, the biomass of phaeocystis can be considered as too low in the base run (Fig. **5**A) when comparing it to the literature data. An increase of alfa for phaeocystis ($alfa_p$; from 0.14 to 0.18 [mmol C m^2 (mg Chl W day)$^{-1}$]), increased the global biomass of phaeocystis (Fig. **5**B) by 40, 50 and 70 % in the three depth layers (0-5m, 5-25m and 25-100m), starting from the surface. Furthermore the NPP of phaeocystis in the AO increased by 59.5 % (data not shown).

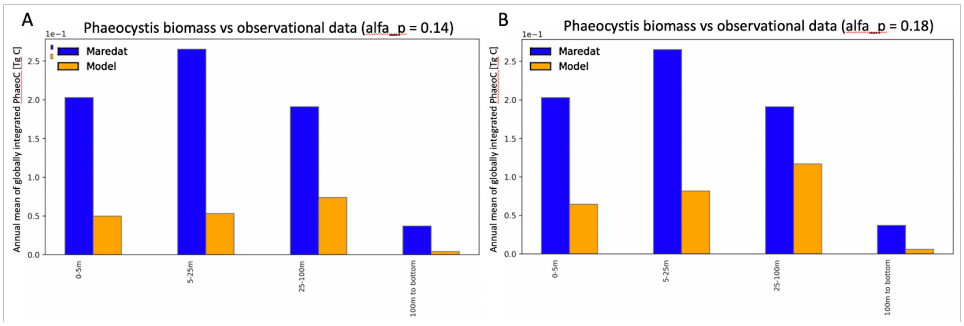

Figure 5: **Global phaeocystis biomass [Tg C] from two different model runs vs observational data from MAREDAT.** A) shows the model output from the baserun using $alfa_p = 0.14$ and B) shows the model output from a tuning-run #22, using $alfa_p = 0.18$. For both runs, output data of the last five years were averaged.

Also, grazing preferences of zooplankton on the single pPFTs were tested and adjusted. In the example shown in Figure **6**, the grazing preference of macrozooplankton on phaeocystis (pzPhaeo2) was increased by 0.5 [unitless], while the one of microzooplankton on phaeocystis (pzPhaeo3) was decreased by 0.5. The distribution of microzooplankton (Fig. **6**B) spreads mainly over the SO and the northern temperate and high latitudes and the equatorial region, while being less prominent in the subtropical gyres. An increase of the microzooplankton biomass of 0.01 Pg C can be observed for the tuned run compared to the baserun, which can likely be located to the SO. Macrozooplankton occurrence (Fig. **6**C) focuses on the SO and only a few regions in the northern hemisphere (south-east of Russia and eastern Canada). Figure **6**A shows an increase in integrated biomass of phaeocystis by 0.02 Pg C from the tuning run over the baserun.

Additionally, grazing parameters from micro- and macrozooplankton

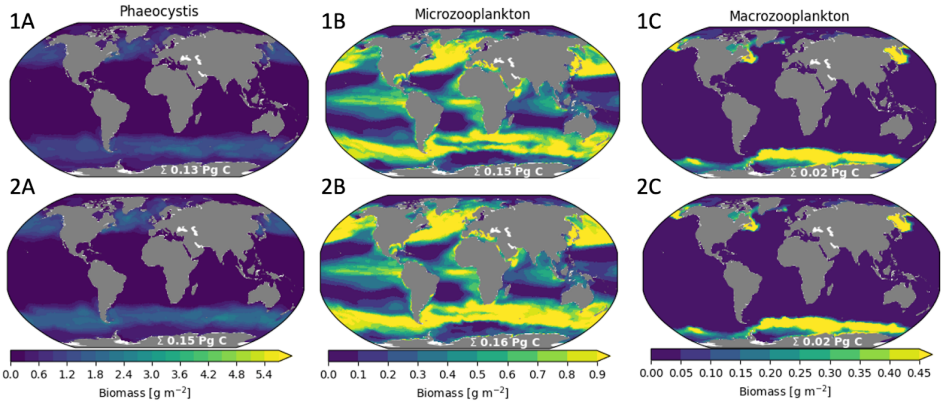

Figure 6: **Integrated global biomass distribution of phaeocystis (A), microzooplankton (B) and macrozooplankton (C).** 1) shows model output from baserun and 2) from a tuning run #26 using an increased grazing preference of macrozooplankton and a decreased grazing preference of microzooplankton on phaeocystis.

($grazMax_3$ and $grazMax_2$, respectively) were tuned in tuning run #36. While the maximum grazing rate for microzooplankton was decreased from 0.46 to 0.36 [mmol N m^{-3} day^{-1}], the one for macrozooplankton was increased from 0.1 to 0.25 [mmol N m^{-3} day^{-1}]. The differences can be observed in Figure **7**B and C (1 shows the model output from the baserun while 2 shows the one from tunging run #36). Microzooplankton biomass shows a general decreased biomass concentration (at 70°N: - 80 %, at 36°N: -42 % and at 50°S: -45 %; Fig. **7**A), while the biomass of macrozooplankton increased (at 70°N: + 535.6 %, at 60°N: +128.4 % and at 60°S: +93.2 %; Fig. **7**C), as expected. The global biomass of microzooplankton decreases from 0.15 to 0.09 Pg C (by 40 %; data not shown), while the macrozooplankton biomass increases from 0.02 to 0.04 Pg C (by 100 %; data not shown). The total zooplankton concentration remains largely unchanged above 50°N while a decrease is observed around 40°N. Around the equator the total biomass decreased slightly as well as in the SO. Even though the grazing parameter of mesozooplankton was not directly modified, an increase of its biomass can be observed around 40°N and 40°S (Fig. **7**B). Globally, it increased from 0.02 to 0.03 (by 50 %; data not shown). Generally, it can be observed that the change of grazing parameters only changes the magnitude of values and does not affect the general distribution. Additionally, the changes of the grazing rates affect the biomass of the pPFTs. While it decreases by 0.02 Pg C (2.5 %), 0.01 Pg C (7,7 %) and 0.07 Pg C (63.6 %) for diatoms, phaeocystis and coccolithophores, respectively, the biomass of small phytoplankton increases by 0.1 Pg C (19.2 %) (data not shown).

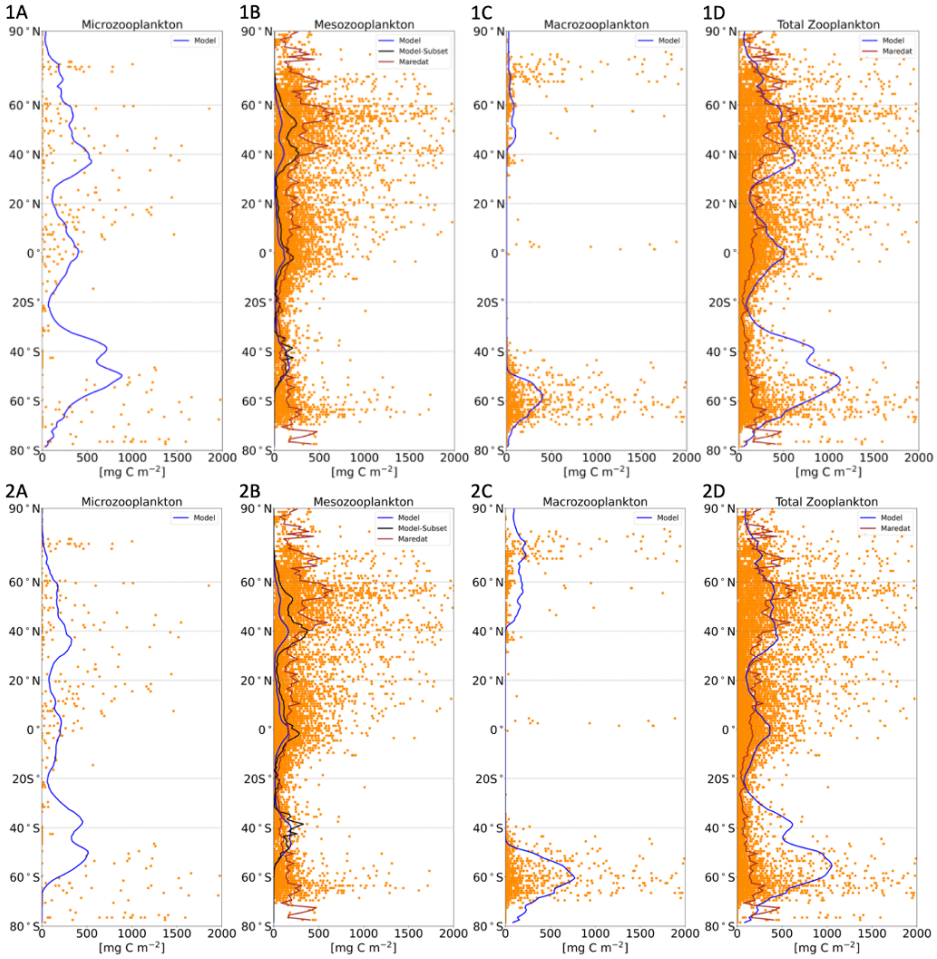

Figure 7: **Latitudinal distribution of depth integrated biomass of zooplankton compared between baserun (1) and tuning run #36 (2).** In tuning run #36 the grazing rates (grazMax) were decreased for microzooplankton to 0.36 (- 0.1) and increased for macrozooplankton to 0.25 (+ 0.15). The single zPFTs (blue) microzooplankton (A), mesozooplankton (B) and macrozooplankton (C) and total (D) were compared to observational data from MAREDAT (orange dots; mean - red line).

The aim of tuning run # 14, 16 and 23 was to investigate the effect of a change in parameters that can influence growth under N-limited conditions, especially in the AO (Fig. **8**). Therefore, in run #14, the maximally allowed Redfield Ratio was increased, leading to a decrease in phaeocystis biomass globally by 0.04 Pg C in total (30 %). Furthermore, the increase of the half saturation constant of phaeocystis $k(din)_p$ did also slightly decrease the phaeocystis biomass by 0.01 Pg C (- 7.7 %). Based on these results, a

decrease in both of those factors would let expect an increase in phaeocystis biomass, however, as shown in Figure **8**D, the model output from run #23 also shows a decrease in phaeocystis biomass in the northern hemisphere. In the SO, an increase can be observed.

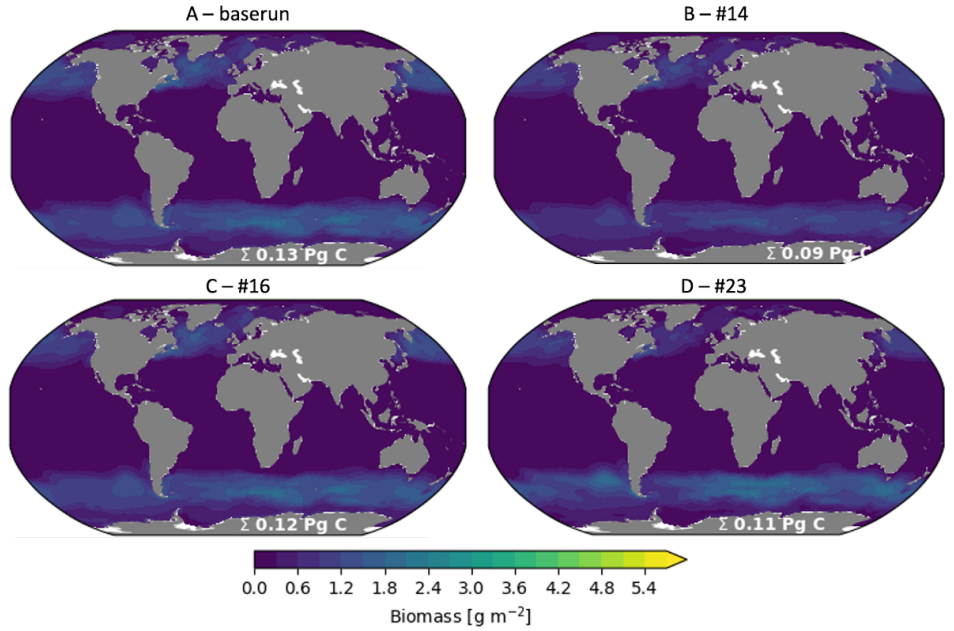

Figure 8: **Global depth-integrated biomass distribution of phaeocystis from different tuning runs.** The different tuning runs aimed to investigate the effect of a increased maximum allowed Redfield ratio (B; tuning run #14; $NCmax_p$ increased by 0.05), increased half-saturation constant (C; tuning run #16; $k(din)_p$ increased by 0.3) and the synergistic effect of the two, when decreasing both (D; tuning run #23; $NCmax_p$ decreased by 0.05, $k(din)_p$ decreased by 0.3). Model output from the baserun is shown in A.

In the tuning process, I further aimed to improve the representation of the phytoplankton community relative to observational estimates by decreasing the dominating high Chl-a concentration of diatoms in the AO. Furthermore, the concentration of small phytoplankton in the polar regions was aimed to be increased, which was too low, likely due to the new temperature functions. Thereby the Chl-a concentration of total phytoplankton was underestimated by the model relative to observations. To increase it, the Chl-a degradation rates and the internal Chl:N ratio were targeted. In run #34, the decrease of the degradation rate (degChl) for small phytoplankton from 0.25 in the baserun to 0.05 [day^{-1}], showed a global increase of phytoplankton biomass by 0.14 Pg C or 27 % (Fig. **9**B). However, also a decrease in other pPFTs was detected (data not shown). Additionally,

degChl of diatoms ($degChl_d$) was increased in tuning run #27 from 0.15 to 0.25 [day^{-1}]. This led to a decrease of diatom biomass of 0.05 Pg C or 6.25 %, while it can be mainly observed in the northern Atlantic Ocean (Fig. **9**C). In tuning run #42 the upper bound for the internal Chl:N ratio of diatoms was decreased from 4.2 to 3.5 [mg Chl mmol N^{-1}]. This shows as well a decrease in diatom biomass mainly in the northern Atlantic Ocean, however, by only 0.02 Pg C or 2.5 %.

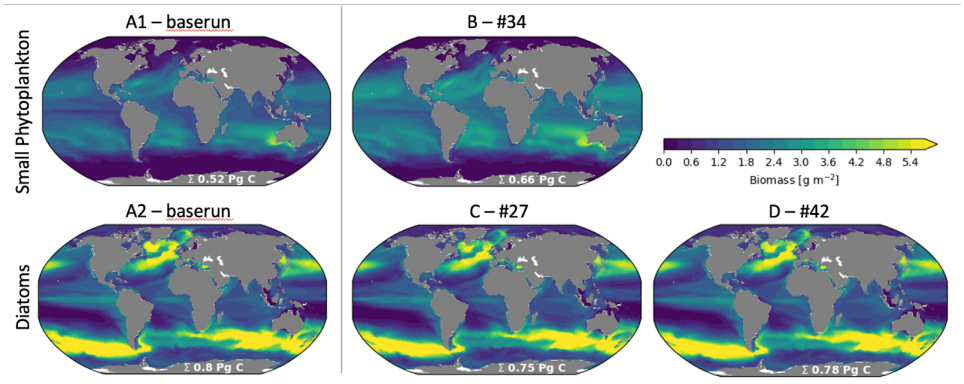

Figure 9: **Global depth-integrated biomass distribution of small phytoplankton (top) and diatoms (bottom) from different tuning runs.** Global depth-integrated biomass distribution of small phytoplankton (top) and diatoms (bottom) from different tuning runs. Baserun (A) is compared to tuning runs #34 (B), #27 (C) and #42 (D). #34 using small phytoplankton Chl-a degradation rate (degChl) of 0.05 [day^{-1}] (- 0.2 compared to baserun), #27 using diatom Chl-a degradation rate ($degChl_d$) of 0.25 [day-1] (+ 0.1 compared to baserun) and #42 uses a decreased upper bound for the internal Chl:N ratio of diatoms ($Chl:Nmax_d$ of 3.5 [mg Chl mmol N^{-1}] (- 0.7 compared to baserun).

3.2 Model Evaluation

For model evaluation, model output of environmental factors from the transient run, such as temperature, salinity, MLD and sea-ice is compared to observational data. Additionally, the ocean productivity and ecosystems were evaluated by looking at global biomass, NPP and Chl-a and nutrients. For NPP and Chl-a an additional focus was set on the AO.
Temperature and salinity statistics comprise a good fit of model output to observational data. This is shown by a SD of 0.993 and 0.997, a r-value of 0.996 and 0.999 as well as a RMSE of 0.090 and 0.044, respectively. The MLD shows in March (AO spring) a strong overestimation of the model in the AO (Fig. **10**/C1), while in September (SO spring) a strong overestimation can be observed in the SO (Fig. **10**/C2). In the rest of the ocean, a

model output represents observational data quite well.
The sea-ice extent decreases over the years from 1979 to 2019 (Fig. **10**D) in both, model output and observational data. While the pattern between model and observational data is very similar, the model overestimates the sea-ice extent by approximately 1.5 million km^2 (21 %).

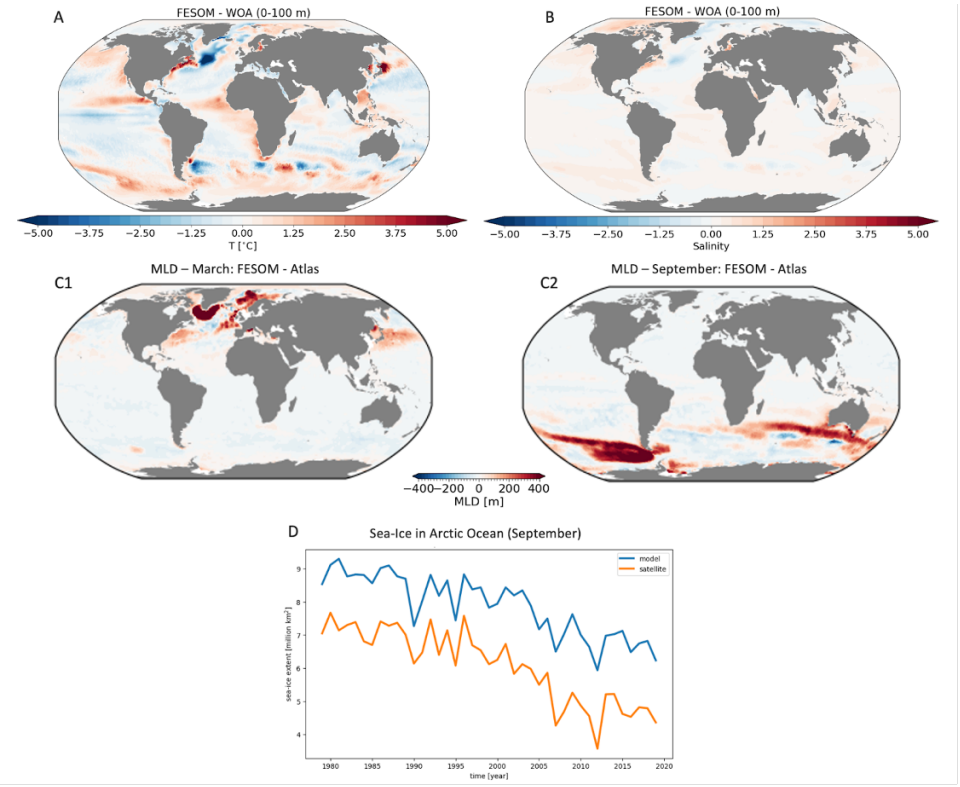

Figure 10: **Comparison of environmental and physical fields between model output and observational data.** Temperature [°C] (A) and Salinity [unitless] (B) is compared to the WOA dataset [9]. Mixed layer depth (MLD, D) [m] is compared to the dataset from Sallée et al. [10]. Sea-ice extent in AO in September [million km^2] is compared to the dataset from the NSIDC [11].

When comparing the nutrient DIN to observational data (Fig. **11**A), underestimation can be observed mainly in the northern Pacific, as well as the northern subequatorial gyre. Especially towards Antarctica and west of South America an overestimation can be seen. The r-value of 0.92, the RMSE of 0.40 and the SD of 1.03, pointing towards an overall well approximation of the observational data. The comparison between observational data and DSi shows a strong overestimation in the SO ($>$ 50°S) of up to 30 mmol Si per m^3. On the other hand, DSi in the northern Pacific is underes-

timated by up to 30 mmol Si per m^3. These spatial misfits are represented by a r-value of 0.90. However, as well as DIN, the model shows also for DSi good fit with observational data by a RMSE of 0.44 and a SD of 0.97.

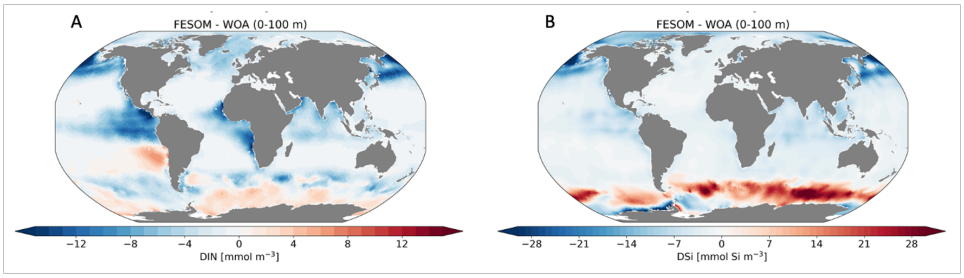

Figure 11: **Differences between model output of global DIN (A) and DSi (B) and observational data.** Model output was integrated over upper 100 m and averaged over the last 11 years of analysis (2013-2023). Observational data was taken from World Ocean Atlas (WOA) dataset [12]. Model overestimations are shown in red, model underestimations in blue.

The global biomass distribution in Figure **12** shows that diatoms occur in the northern Atlantic and Pacific Ocean as well as the southern Pacific and Indian Ocean with their biomass summing up to 0.61 Pg C. Small phytoplankton range more consistently in more temperate waters and are non-existent towards the poles with a sum of 0.78 Pg C. Coccolithophores biomass is with 0.13 Pg C globally lower than the biomass of diatoms and small phytoplankton. It ranges in the SO from the Atlantic Ocean to the south of Australia. In the northern hemisphere, they occur in the northern Atlantic and Pacific Ocean, without occuring in latitudes $>$ 70°N and $>$ 60°S. Phaeocystis only occurs in colder waters above 40°N and and 30°S, showing a continuous distribution there. They sum up to 0.13 Pg C.

Figure **13** shows the latitudinal distribution of NPP and Chl-a of the pPFTs compared to observational data. It shows diatom Chl-a and NPP mainly at latitudes above 30°S and 30°N, while small phytoplankton dominate in the subtropical gyres and the equator. Coccolithophore NPP and Chl-a can be observed at the equator and at approximately 40°S and 30 - 50°N.

The model output data of Chl-a approaches the observational data well in the subtropical gyres, while it underestimates the NPP. However, NPP in the subarctic regions are well met. The Chl-a profile shows an underestimation of the model regarding Chl-a and NPP, especially in the AO, but also Chl-a in the SO. When looking at the global Taylor statistics of Chl-a, a rather low r-value of 0.45 can be observed, while the RMSE has a high value of 0.97. The SD is 0.84. The statistics of the global NPP, when compared to VGPM, has values of 0.30, 1.29 and 1.17 for the r-value, RMSE and SD, respectively. When compared with CbPM, r has a value of 0.07, RMSE of

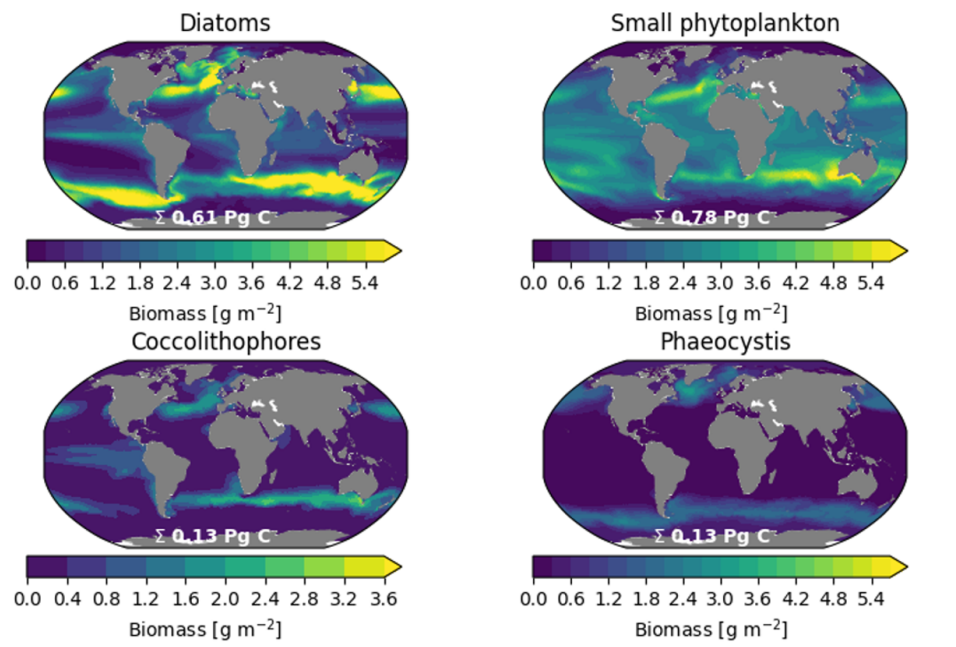

Figure 12: **Global distribution of vertically-integrated phytoplankton biomass.** Calculated in the transient simulation, vertically integrated and averaged over the last 11 years (2013-2023) for the four pPFTs, (A) diatoms , (B) small phytoplankton, (C) coccolithophores and (D) phaeocystis.

1.51 and SD of 1.21.

When comparing the NPP in the AO to both, the observational data from Lewis et al. [17] and GlobColour, an overestimation of the model in the Greenland Sea (east of Greenland) and at the coastlines can be observed. However, the intensity of the overestimation varies between the two datasets.

Also, an overestimation of Chl-a on the coastlines can be observed for both Chl-a datasets, Lewis et al. [17] and OC-CCI, while it is much greater for the OC-CCI dataset. Furthermore, an underestimation of Chl-a can be observed in the Barent Sea (north of Eurasia) and Greenland Sea, while Chl-a in the Norwegian Sea is overestimated. This pattern can be observed in comparison to both datasets, however, when compared to Lewis et al. [17] the coastal areas are better approximated than when compared to the OC-CCI dataset. Taylor statistics in the AO of Chl-a compared to Lewis et al. have values of 0.04, 1.14 and 0.58 for r, RMSE and SD, respectively. These are similar to the statistics when comparing to the OC-CCI dataset: -0.3, 1.3 and 0.58 for r, RMSE and SD, respectively. For NPP in the AO, statistics are generally better with a r-value of 0.70 and 0.68, a RMSE of

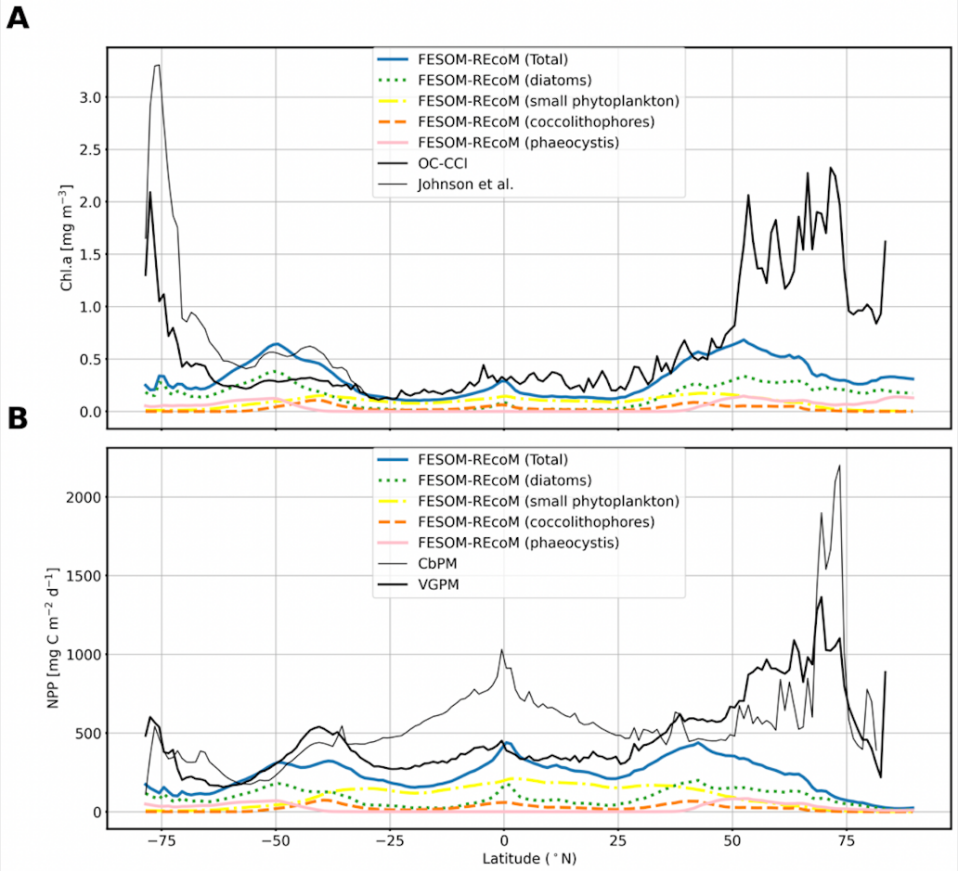

Figure 13: **Latitudinal distribution of Chl-a (A) and NPP (B)** of the four pPFTs in REcoM3 (total (blue), SmallPhy (yellow), diatoms (green), coccolithophores (orange) and phaeocystis (rose)) compared to observational data. Chl-a (A) in the SO was compared to Johnson et al. [13] (grey) and the OC-CCI dataset [14] (black). NPP (B) is compared to CbPM (grey) [15] and VGPM (black) [16]. The latitudes range from 80°S (SO) to 90°N (AO).

0.71 and 0.74 as well as an SD of 0.66 and 0.81 when comparing to Lewis et al. [17] and GlobColour, respectively.

3.3 Hindcast Simulations

Furthermore, the output from the transient run was used to investigate the development of plankton ecosystems globally and in the AO. For this, first of all a timeseries was plotted (Fig. **16**) which shows that the total NPP of the four pPFTs is decreasing globally by 2 Pg C (relative trend = - 6.25 %; 2A) but increases in the AO by 33 Tg C (relative trend = 22.98 %; 2B). A

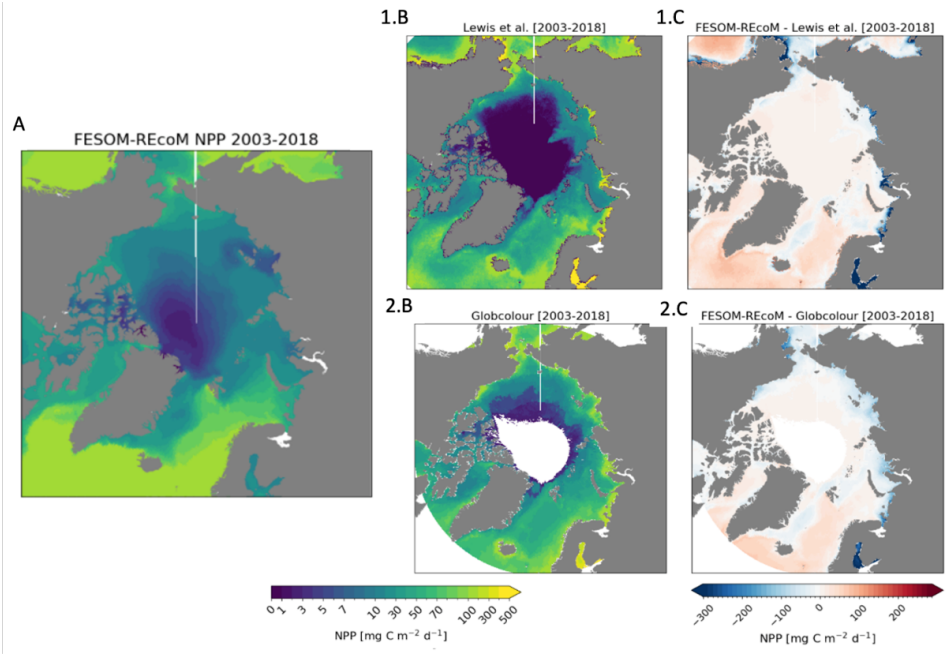

Figure 14: **Arctic Ocean vertically-integrated total NPP.** Model output (A) from the transient simulation is compared to observational data from Lewis et al. [17] (1B, C) and the GlobColour dataset (2B, C) to show discrepancies between model simulation and different observational data. Differences between observational data and model output is shown in C.

closer look was taken on the behavior of NPP of phaeocystis (Fig. **16**/1A and 1B), which pattern coincides with the one of total NPP. Phaeocystis NPP decreases in the global ocean by 0.079 Pg C (relative trend = - 5.32 %; 1A) and in the AO increases by 18 Tg C (relative trend = 36.06 %; 1B). Also the C-export flux decreased in the global ocean over the years from 1970 to 2023 by 1 Pg C (relative trend = - 18.5 %; 3A). Interestingly, while NPP increases in the AO, the C-export flux shows a negative trend of - 7.45 % (1.1 Tg C).

Figures **17** to **20** show absolute and relative trends over the 54 years of the analysis period from 1970 to 2023 in NPP and Chl-a. An overview of the arctic subregions that are used for description of the figures in the following, is shown in Appendix .1. Figure **17** shows an increase of absolute total NPP in the Greenland Sea (east of Greenland) and Barent Sea (north of Eurasia) and southern Baffin Bay (between Canada and Greenland) of over 0.7 g C per year in combination with a decrease of over 0.5 g C per year in the northern Baffin Bay and coastal areas (Fig. **17**A). Furthermore, an increase is observed in the Arctic-Canadian Archipelago.
This pattern correlates with the one of the NPP of diatoms and phaeocystis.

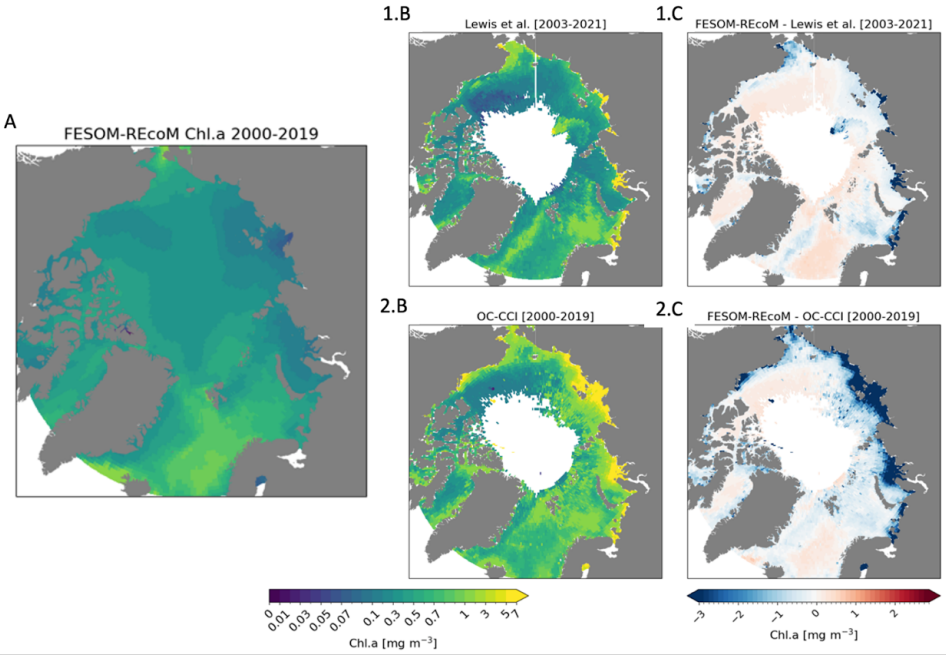

Figure 15: **Arctic Ocean total surface Chl-a in summer.** Model output from June to October (A) from the transient simulation compared to observational data (B) from 1) Lewis et al. [17] and 2) the OC-CCI dataset to show discrepancies between different observational data. Differences between observational data and model output is shown in C.

Also, the increase of NPPp at 70 - 80°N, observed in Figure **17**B, can be observed in the relative trend of phaeocystis NPP in Figure **18**E (up to 4 % per year). Additionally, absolute and relative trends of phaeocystis Chl-a align with the NPP signature of phaeocystis (Fig. **19**/ **20** E).
Diatoms decrease in the central AO, when looking at the relative trend (Fig. **18**C) by up to 3.5 % per year. Apart from this, the pattern seen in the absolute changes can also be observed in the relative trend of diatoms (Fig. **18**C) and phaeocystis (Fig. **18**E). NPP of small phytoplankton increases throughout the AO, even more dominant in the relative comparison (Fig. **17**/ **18** B). While coccolithophores do not show an absolute increase/decrease in the AO, it shows a strong relative increase of over 10 % in the Greenland Sea, the Barent Sea, the Baffin Bay, north of Russia and Alaska.

The same trend maps were plotted for the C-export flux – first, at 100 m depth (Fig. **21**/1), as this is used for global ocean evaluations, and second, at 30 m depth (Fig. **21**/2) to capture the export in the AO, closer to the shelfs. The relative C-export flux trend of both depths (Fig. **21**A) shows a

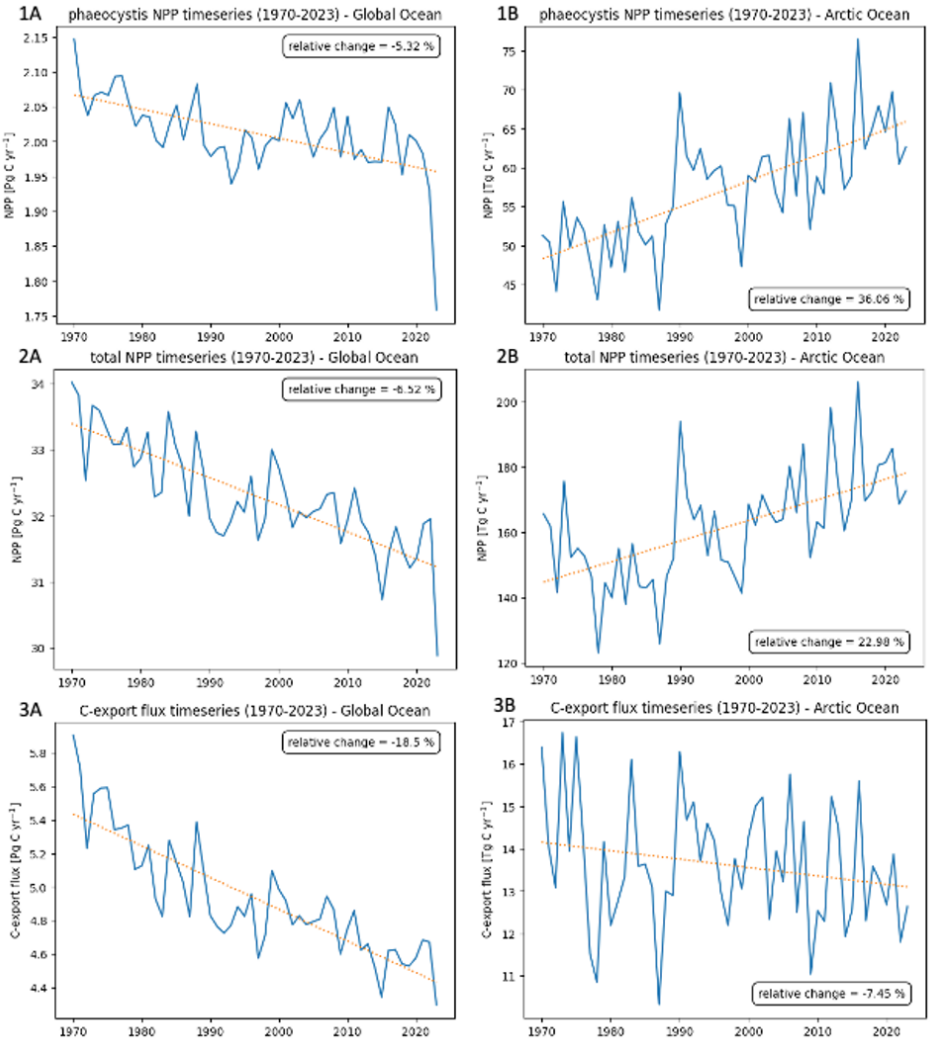

Figure 16: **Time-Series of 1) phaeocystis NPP, 2) total NPP and 3) C-export flux globally (A) and in the AO (B) from 1970 to 2023.** Model output data was averaged over the specified region per year and is shown in blue, while a linear trend was calculated using the polyfit function from numpy and plotted in orange. The relative change between the first year (1970) and the last year (2023) was calculated and shown in the box. Note the different scales on the y-axis between the plots.

decrease in the central AO, but an increase in the regions where a higher NPP and Chl-a of pPFTs is observed – in the eastern Greenland Sea and in the northern Barent Sea. In these regions an increase up to 2 % per year can be observed at a depth of 100 m. A strong increase of 4-5 % per year can be observed in small areas in the Canadian Archipelago. On the other

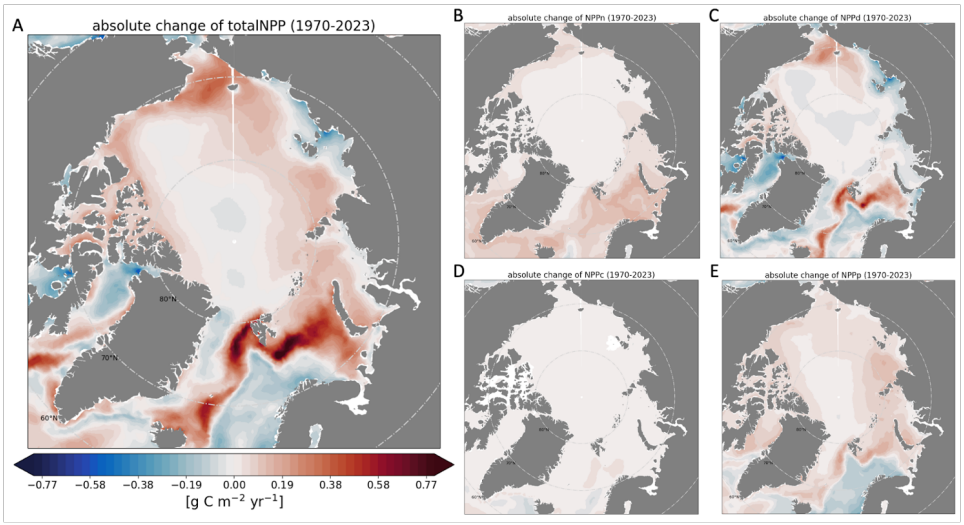

Figure 17: **Absolute changes of depth-integrated NPP [g C m^{-2} yr^{-1}] in AO (1970-2023).** The absolute trend of total NPP (A), small phytoplankton NPP (NPPn; B), diatom NPP (NPPd; C), coccolithophore NPP (NPPc; D) and phaeocystis NPP (NPPp; E) is calculated using the linear regression using polyfit function from numpy.

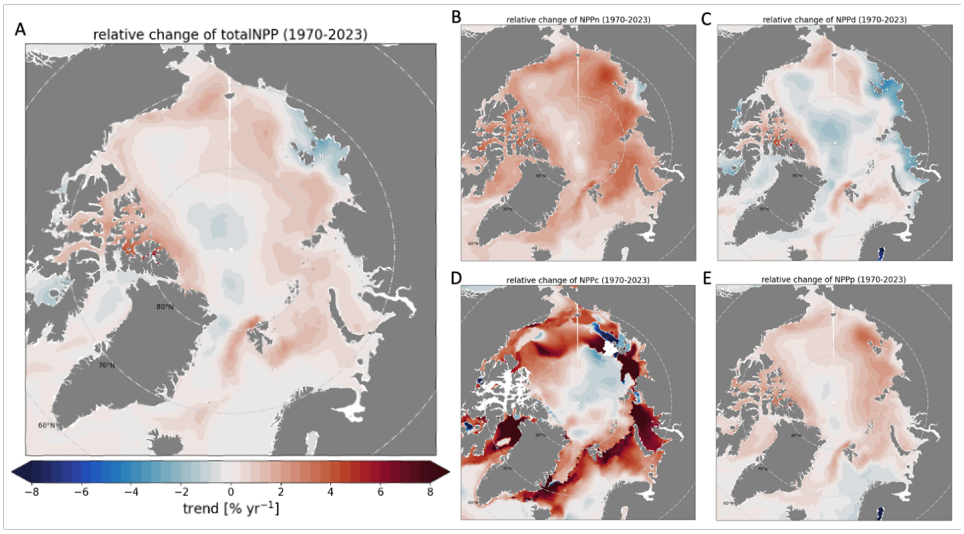

Figure 18: **Relative changes of NPP [% yr^{-1}] in the AO (1970-2023).** The relative trend of total NPP (A), small phytoplankton NPP (NPPn; B), diatom NPP (NPPd; C), coccolithophore NPP (NPPc; D) and phaeocystis NPP (NPPp; E) is calculated by taking the difference between the linear regression's first year and last year value and dividing it by the first year value multiplied by the years and finally multiplied by 100 %.

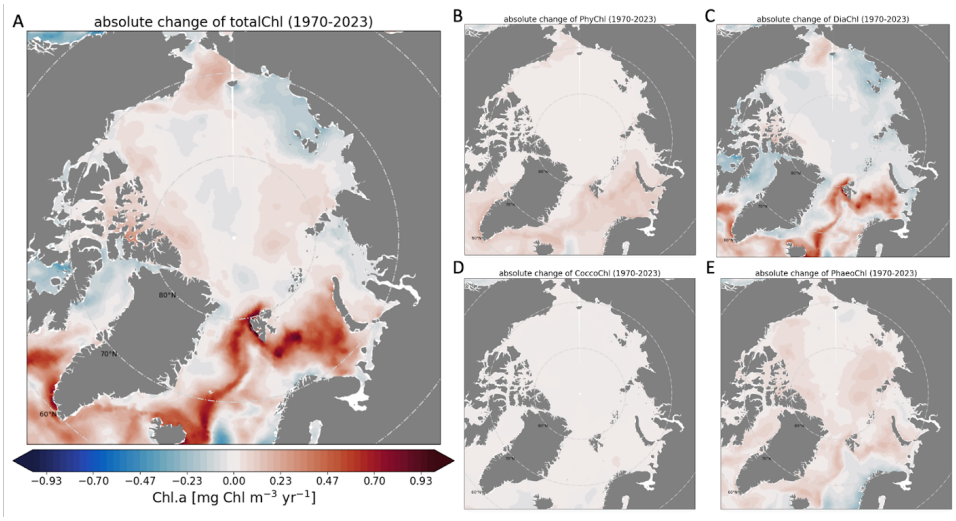

Figure 19: **Absolute changes of Chl-a [mg C m^{-3} yr^{-1}] averaged over upper 100 m in AO (1970-2023).** The absolute trend of total Chl-a (A), small phytoplankton Chl-a (PhyChl; B), diatom Chl-a (DiaChl; C), coccolithophore Chl-a (CoccoChl; D) and phaeocystis Chl-a (PhaeoChl; E) is calculated using the polyfit function from numpy.

hand, the C-export flux in the overall central AO is decreasing up to 1.4 % every year (at 30 m and 100 m depth). A similar trend can be observed in the Baffin Bay, the Norwegian Sea, where strongly negative absolute trends can be observed. In the Baffin Bay, a negative trend of diatom NPP dominates the positive trend of the other three pPFTs hence the total NPP trend remains negative and so does the C-export flux. C-export flux at 30 m depth in the AO is evaluated in Figure **21**/2 and shows an increase of up to 1.5 % per year in the Chukchi Sea. Coastal regions of the East Siberian and Laptev Sea can still not be captured due to shelfs, shallower than 30 m.

To investigate possible causes of NPP, Chl-a and C-export flux trends, absolute trends of environmental factors such as surface temperature, sea-ice cover (SIC) and available light (PAR) were investigated (Fig. **22**A, B and C). Relative trends are shown in Appendix .3. Temperature shows an increase towards the Atlantic Ocean (Fig. **22**A), where simultaneously an increased sea-ice melt occurs (up to 6 % of SIC per year in the eastern Greenland Sea and up to 9 % per year in the northern Barent Sea; Fig. **22**B). Additionally, the light availability is increasing in these regions, but mainly in coastal areas of the AO (Fig. **22**C), where no strong negative relative trend of sea-ice coverage or temperature is detected.
Furthermore, the trends of the nutrients DIN and DSi (Fig. **22**D and E, respectively) were analysed. Both show a decrease. DIN decreases up to 0.08 mmol m^{-2} per year (3.3 % per year) in the Siberian Sea while DSi decreases

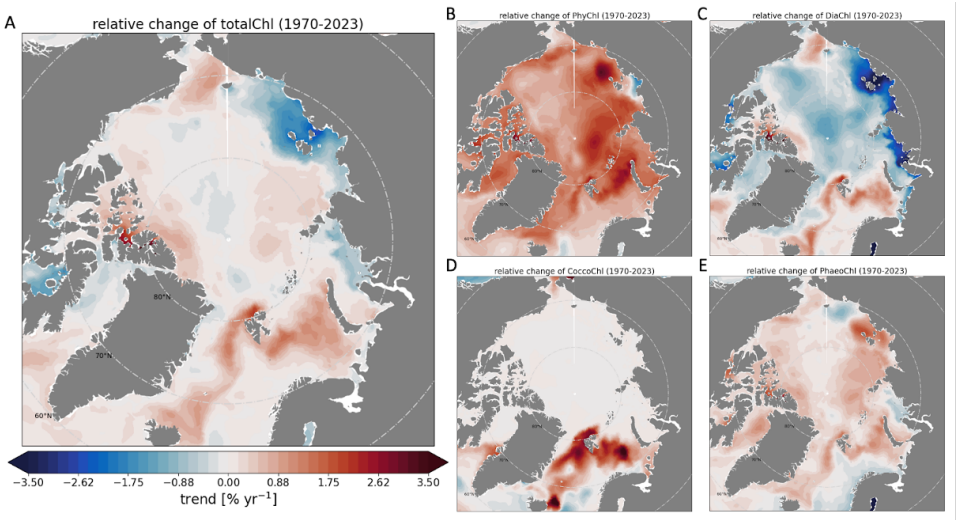

Figure 20: **Relative changes of Chl-a [% yr^{-1}] averaged over upper 100 m in AO (1970-2023).** The relative trend of total Chl-a (A), small phytoplankton Chl-a (PhyChl; B), diatom Chl-a (DiaChl; C), coccolithophore Chl-a (CoccoChl; D) and phaeocystis Chl-a (PhaeoChl; E) is calculated by taking the difference between the linear regression's first year and last year value and dividing it by the first year value multiplied by the years and finally multiplied by 100 %.

up to 0.15 mmol m^{-2} per year (approx. 4 % per year) in the Siberian Sea, Canadian Archipelago and the coast of Greenland. No outstanding decrease is observed in the eastern Greenland Sea and northern Barent Sea where there is a significant increase of total NPP. Also the MLD was investigated (Fig. **22**F). In the eastern Greenland Sea an increase in depth of up to 4.5 m per year can be detected. Also, an increase in depth can be observed for the central AO (relative trend = + 0.88 %).

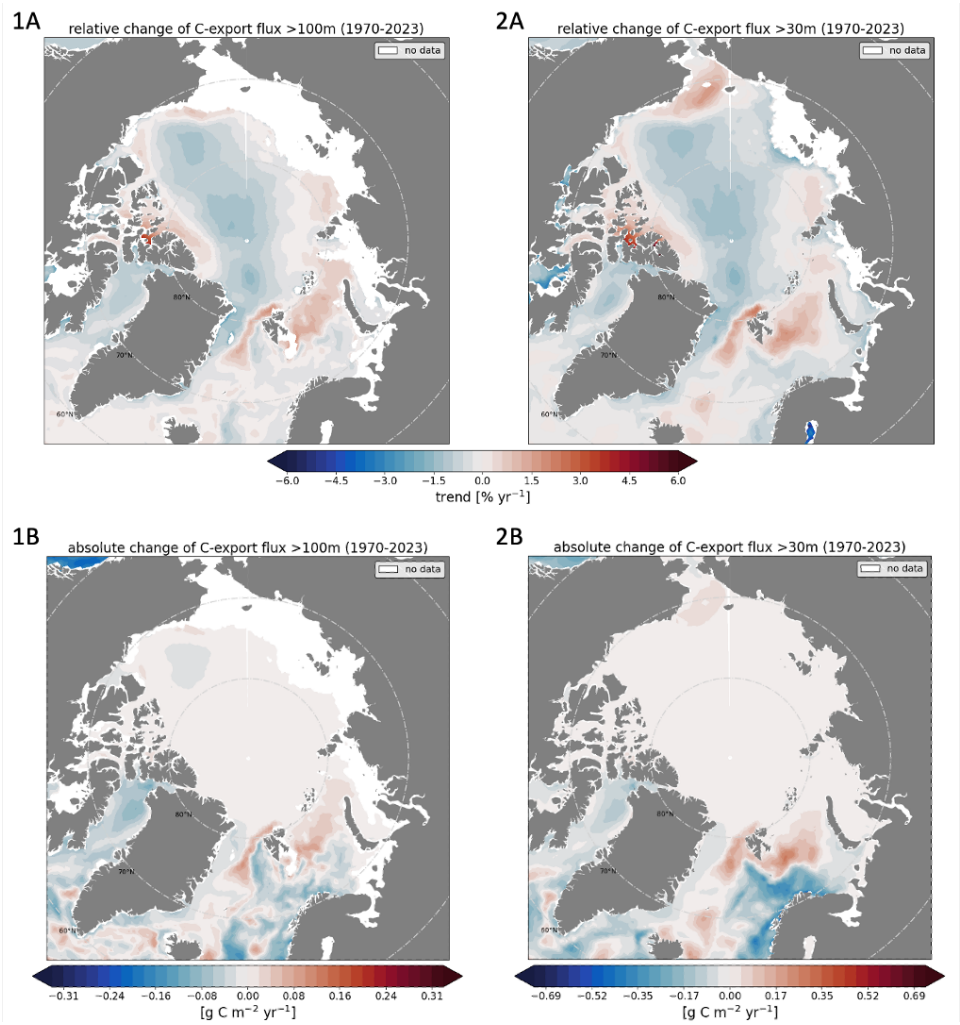

Figure 21: **C-export flux trend in the AO at 100 m depth (1) and 30 m depth (2).** Relative trends (A) are given in [% yr^{-1}] and absolute trends (B) in [g C m^{-2} yr^{-1}]. Areas where depth is lower than 100 m or 30 m, respectively, have no data about export and are shown in white.

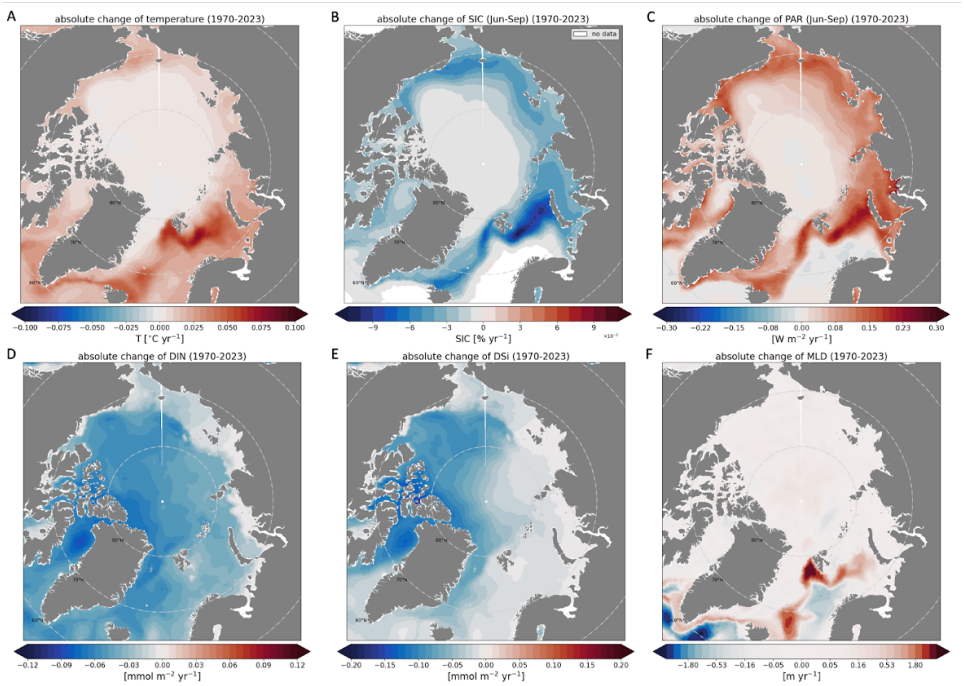

Figure 22: **Absolute trends of environmental factors and nutrients in the AO (1970-2023).** Temperature [°C yr^{-1}] (A), sea-ice coverage (SIC) [% yr^{-1}] (B), PAR [W m^{-2} yr^{-1}] (C) are only plotted for the surface layer, while SIC and PAR only represent the trend of the summer months (Jun - Sep). DIN (D) and DSi (E) in [mmol m^{-2} yr^{-1}] were averaged over the upper 100 m. The mixed-layer depth (MLD, F) is given in [m yr^{-1}].

4 Discussion

4.1 Tuning Strategy

The tuning processes of the model parameters aimed to improve the representation of biological and biogeochemical signals after the addition of one pPFT and the implementation of new temperature functions for phytoplankton growth. After the initial selection of parameter values from literature estimates, these parameters were modified for reruns, separately and in combination, to get the model results closer to the observational data. During the tuning process, I could observe direct and indirect effects of the parameter choice on the model output, thereby gradually improving the fit of the model results to observational data. A detailed description of these steps as outlined below will help future tuning attempts of REcoM to more specifically target those parameters that have the largest effect on certain biological and biogeochemical signals.

In the output of the baserun which used the first set of parameter estimates, I observed that the global biomass of phaeocystis (0.13 Pg C) is too low compared to the observational MAREDAT data. To address this deviation, several parameters were tuned, such as alfa (the initial slope of the photosynthesis-irradiance curve) and the grazing preferences.

In this study, the phaeocystis biomass was identified to be particularly sensitive to the photosynthesis parameter alfa, as an increase of $alfa_p$ by 0.04 (initial value: 0.14) lead to an increase in global surface biomass by 40 % (Fig. **5**) and global depth-integrated NPP by 41.2 %. In the AO an increase of phaeocystis NPP of 59.5 % was observed (data not shown). Regarding these results it can be concluded that, when alfa is increased, the light harvesting efficiency is increased for low light, hence resulting in more NPP and biomass, especially in regions of extreme light conditions such as the AO.

When adjusting the grazing preferences of zooplankton on phaeocystis, one can observe that a decrease in microzooplankton grazing preference on phaeocystis (pzPhaeo3) is increasing the global biomass of phaeocystis by 0.02 Pg C (initial value: 0.13), even though the grazing preference of macrozooplankton on phaeocystis (pzPhaeo2) was increased. This can be explained by the required regional overlap of prey and predator (Fig. **6**), which is less for macrozooplankton and phaeocystis especially in the AO but also in parts of the SO (southwest of South America). Furthermore, in regions of overlap there is still an increase of phaeocystis. This can be due to the rather low biomass of macrozooplankton of 0.02 Pg C, which

is only 12.5 % of the biomass of microzooplankton. Interestingly, by decreasing pzPhaeo3, also the biomass of microzooplankton is increased by 0.01 Pg C. One factor influencing this might be the increased food supply by increased phaeocystis biomass, assuming food is a main limiting factor for microzooplankton growth. Simplified, this means that if the grazing preference of microzooplankton on phaeocystis is decreased, the same phaeocystis biomass can sustain (or feed) a higher biomass of microzooplankton, as microzooplankton grazes more on prey other than phaeocystis. Additionally, as macrozooplankton feeds more on phaeocystis, the feeding on microzooplankton might be reduced, causing an increase in microzooplankton biomass. Overall, the equilibrium is, however, still on the side of the prey (phaeocystis) as it increases in biomass compared to the baserun. This means the sink term (grazing pressure) is still smaller than the source term (growth), hence, phaeocystis still has a net increase. However, further investigations would be required that includes all grazing interactions (for example also the grazing of macrozooplankton on microzooplankton) and feedbacks to test these hypotheses. This will not be covered in this thesis. Additionally, to address the difference between zPFTs of how much they graze hence build biomass, the grazing rates (grazMax) were decreased and increased for microzooplankton and macrozooplankton, respectively (Fig. **7**). This allows for a higher grazing pressure of macrozooplankton on the pPFTs and a reduced grazing pressure of microzooplankton on phaeocystis, diatoms and coccolithophores. The indirect changes in biomass of mesozooplankton may be explained by the increase in food supply for mesozooplankton in areas where microzooplankton became less prominent. This directly triggers a strong decrease of 63.6 % of coccolithophore biomass, as the grazing preference of mesozooplankton on coccolithophores (pzCocco2) in the baserun is 0.666, while the grazing preference of microzooplankton on coccolithophores is zero. The preference of micro- and mesozooplankton on small phytoplankton is 0.5 for both, hence an increase in small phytoplankton biomass can only be explained by less overlapping regions of small phytoplankton and mesozooplankton where they could meet. These findings about the interactions between grazing preferences, grazing rates and biomass are crucial to keep in mind when adjusting the grazing rates and preferences in order to increase the pPFT biomass.

As this study focuses on the implementation of phaeocystis in the AO, an N-limited environment, it is important to look at the parameters controlling the behaviour under N limitation. To do so, the upper bound of the N:C ratio was increased (decreased Redfield C:N ratio from 6.6 to 5), allowing for less growth under the same nitrogen conditions. As expected, this decreases global biomass of phaeocystis (Fig. **8**B). Additionally, the half-saturation constant of N for phaeocystis ($k(din)_p$) was increased. The higher it is, the less nitrogen can be taken up at low concentrations, meaning

reduced growth at low N concentrations. This is reflected in the results by a decrease in phaeocystis biomass (Fig. **8**C). According to these outcomes, a tuning run with a decrease of both, N:Cmax_p and k(din)$_p$, was conducted. Surprisingly, this decreased the phaeocystis biomass by 15.4 %. This shows that some feedback processes are not straight forward, making it vital to test and investigate unexpected synergistic effects.

One detail that can be observed for the biomass distribution in model output from the baserun, is that the small phytoplankton PFT vanishes north of Russia and Canada and at latitudes higher than 60°N. As this was also observed, without the implementation of phaeocystis, it is likely due to the new temperature function used for small phytoplankton. To counteract this effect, the Chl-a degradation rate of small phytoplankton (degChl$_n$) was addressed by decreasing it (tuning run #34). This successfully increased the biomass of small phytoplankton by 26.9 % (Fig. **9**B). Additionally, small phytoplankton appeared in higher latitudes like the south of Greenland and in the Norwegian Sea, where it was not represented in model outputs from the baserun. This can be explained by the role of Chl-a in the internal stoichiometry of a pPFT, C:N:Chl. A lower degradation rate of Chl-a reduces Chl-a loss (see Eq. 12), hence increasing intracellular Chl-a and the amount of photosynthesis that can be performed, leading to growth / an increase in biomass. On the other hand, an increase of degChl of diatoms (degChl$_d$) is decreasing the internal concentration of Chl-a hence reducing growth (Fig. **9**C). This was tested in tuning run #27 to reduce the, in the model, dominating pPFT diatoms, which was successfully decreased globally by 6.25 % over the baserun. The decrease can visually be located especially to the northern hemisphere. To further limit diatom biomass, specifically in the AO, the upper bound for the internal Chl:N ratio of diatoms (Chl:Nmax_d) was decreased by 0.7 (tuning run #42). This also led to a decrease in global diatom biomass by 2.5 %, which can be mainly located to the AO again (Fig. **9**D). The stronger limitation of Chl-a to the limiting nutrient in the AO (N) influences the synthesis of Chl-a by being a multiplying factor in the Chl-a synthesis term (see Eq. **8**). When intracellular Chl-a is decreased, the photosynthesis rate is decreased, hence, less growth and lower biomass. However, this tuning run showed a less strong effect compared to the tuning run #27, which did address degChl$_d$.

These tuning runs provided useful knowledge of the impacts of the single parameters and interactions between input parameters and model output. Based on these findings, the most promising investigated parameter changes were combined in another run and checked for synergistic effects. A run with tuned temperature functions performed by Hannah Haines (#39) was finally used and combined with the following parameter changes (see Table 1 for parameter values used for final runs):

- increased alfa for phaeocystis and small phytoplankton
- decreased grazing preference of microzooplankton on phaeocystis (pzPhaeo3)
- changed general grazing rates of micro- and macrozooplankton
- increased grazing preference of microzooplankton of coccolithophores (pzCocco3)
- altered Chl-a degradation constants for diatoms and small phytoplankton

For phaeocystis, a final value for alfa of 0.17 was chosen to keep the balance between diatoms ($alfa_d = 0.18$) and small phytoplankton ($alfa_n$=0.15). The half saturation constants of N ($k(din)_p$), as well as N:Cmax remained unchanged due to unclear feedbacks in the model. This would require further research to understand these feedbacks better. For now, the values were chosen based on compromising values of the other pPFTs and literature values of phaeocystis while keeping the nitrogen limitation in the AO in mind. The grazing preference of microzooplankton on phaeocystis was further decreased to 0.25 [unitless], as this study focuses on a colony forming species and colonies are unlikely to be grazed by microzooplankton. However, grazing on single cells remains, why it was set to a value larger than zero. The grazing preference of macrozooplankton on phaeocystis was increased to 1.0 [unitless]. The grazing preference of mesozooplankton on phaeocystis was kept at the initial value at 0.5 [unitless]. However, as the tuning runs showed that an increased grazing preference of macrozooplankton is not enough to increase the grazing pressure on phaeocystis, the grazing rate of macrozooplankton was increased, while the one of microzooplankton was decreased.

In the new model version established in this study, coccolithophore biomass was increased by using its new temperature function (data not shown and discussed here). Furthermore, the general grazing rate of microzooplankton was decreased. To keep coccolithophores under control, the grazing preference of microzooplankton on coccolithophores was adjusted to 0.5 (was zero before).

Lastly, the Chl-a degradation constants for diatoms and small phytoplankton were adjusted in order to account for changes mainly by the new temperature functions.

4.2 Model Evaluation

To evaluate the final tuned model, model output from the transient run (i.e. sea-ice, temperature, MLD, nutrient patterns from DIN and DSi, biomass,

Chl-a and NPP) were compared to observational data. From this it can be concluded that a good approximation to observational data was achieved by the model.

The final tuned model version is overall representing temperature, salinity, MLD and nutrients well (Fig. **10** and **11**). Low RMSE values (0.090, 0.044, 0.4 and 0.44 for temperature, salinity, DIN and DSi respectively) point towards a low distance from model output data to the reference point. High r-values (0.996 and 0.999, 0.92 and 0.9 for temperature, salinity, DIN and DSi respectively) mean that also the spatial pattern is represented well and SD values close to 1 point towards a good representation of the variability of the observational data. Some biases in MLD remain compared to the 2pPFT-version by Gürses et al. [42]. Among them are the overestimation south of Greenland as well as the Norwegian and Greenland Sea in March and the overestimation in the southern Pacific and Indian Ocean in September (Fig. **10**/C1 and C2). This is due to stronger mixing of the waters by storms in the winter months (AO – March, SO – September). However, overall the global representation of MLD is reasonable. When looking at the comparison of the timeseries of sea-ice extent in the AO, the pattern fits well, while the model is generally overestimating it. This is a common problem in many models. West and Blockley [67] suspect that this might be due to biases in the parametrization of sea-ice thermodynamics. When looking at the nutrients, DIN and DSi show a higher RMSE, meaning a higher discrepancies between model output and observational data, likely due to a slight spatial disagreement, indicated by a r-value of 0.92 and 0.90, respectively. For DIN, the reason for this could be the negative bias up to 13 mmol per m^3 in the sub-Arctic regions. This bias is also occurring in the previous version of REcoM [42] and is likely caused due to issues in representing circulation in some regions of the model (personal communication with Qiang Wang. Furthermore, DSi is strongly overestimated in the SO, which also didn't change compared to the 2pPFT-version of Gürses et al. [42]. As changes in the silicate bias are highly linked with the productivity of the silicifying diatoms, one reason for this positive bias might be the overestimation of the recycling and dissolution of silicate after a bloom [68].

When evaluating the biomass distribution of the single pPFTs using Figure 12 and 13, it fits well to the distribution from the 3pPFT-version from Seifert et al., [3]. For example, the main distribution of coccolithophores is in the north Atlantic and southern Indian Ocean. Small phytoplankton occur mainly in more temperate waters. However, in the 3pPFT-version [3], they additionally reach latitudes over 60°S and all the way to the sub-Arctic region, which is not the case in the model version of the present study. This difference can likely be explained by the new temperature functions used, which reduces the concentration in the AO. Additionally, the polar

pPFT phaeocystis is 'split off' from the small phytoplankton group in the 4pPFT-version, hence reduces the amount of small phytoplankton in the polar regions.

When evaluating the total global Chl-a and NPP, relatively high RMSEs (0.97 and 1.29, respectively) point towards a high variance between modeled and observational data. A SD of 0.84 for Chl-a means a slight underestimation of the variance of the observational data, while it is overestimated for NPP (SD = 1.21). The low r-values of 0.45 and 0.3, respectively, point towards regional misfits. These regional misfits can be located via the latitudinal plot (Fig.13) and a plotted global map distribution (not shown) to the polar regions. When looking at figures 14 and 15, showing AO Chl-a and NPP differences to observational data, a negative bias (underestimation) of both can be observed in the coastal regions. There, observational data are known to have a positive bias, meaning observational models are overestimating Chl-a and NPP. A reason for this is the absorption of CDOM and SPM, which are most prominent in coastal areas due to riverine input [60]. When comparing two different sources of observational data in figures 14 and 15, the overestimation is stronger when compared to GlobColour (NPP) and OC-CCI (Chl-a) data than when compared to Lewis et al. [17]. Reason for this is that Lewis et al. [17] corrected for CDOM and SPM using observational data.

Overall, the new model version is approximating environmental and physical factors well. Simulations of NPP and Chl-a show limitations compared to observational data. However, observational data often derives from remote sensing models or field observations with limited regional and temporal availability. However, even though this makes the representation of NPP and Chl-a in a model difficult, a good approximation was established here, while keeping model and observational data limitations in mind. As this tuning strategy aims for a good representation of the global ocean with a focus on the AO, evaluation for the SO would be required and may include minor tuning in the future.

4.3 Hindcast Simulations

The evaluated transient runs were also used to branch off the so-called 'hindcast simulations'. As the model is only in a 'quasi'-steady state, the first years from 1958 to 1969 were omitted for the trend analyses, as they still showed strong variations between years. For the analysis period from 1970 to 2023, biomass, NPP, Chl-a and nutrients trends were plotted. This showed a shift in the phytoplankton community, where diatoms increased less than small phytoplankton and the haptophytes coccolithophores and phaeocystis.

4.3.1 Physical and Environmental Trends

When comparing the trend of temperature from 1970 to 2023 in the AO (Fig. **22**A), an increase between 0.05 and 0.1 °C per year can be observed, which is a change of up to 0.5 - 1 °C per decade (yearly average) in the northern Barent Sea and north-east Greenland Sea. In the IPCC Special Report on the Ocean and Cryosphere in a Changing Climate [26], temperature trends between 1982 and 2017 showed an increase of 0.5 °C per decade in September and 0.25 °C per decade in March in the same region. Even though in this study, a longer period as well as the yearly average was analyzed, a slight overestimation can be suggested in the region. When comparing the temperature trend in the Chukchi Sea, in this study an increase of up to 0.25 °C (yearly average) per decade can be reported. In this region, the IPCC report reports a change of 0.5 °C in September, which shows a good approximation from model data, whose yearly average is 0.25 °C per decade.

However, conclusions are difficult to draw as different trend calculations were performed. While the IPCC report only reports temperatures from ice-free regions in relation to sea-ice melt, in this study the trends also include ice-covered regions. Changes in sea-ice are reported to be -12.8 % in September (the month when the yearly minimum of sea-ice coverage is reached). Peak declines are ranging from the Beaufort Sea, over the Chukchi Sea to the East Siberian Sea. In this study (Appendix .3), - 6 % relative change of sea ice coverage in the summer months (June to September) can be observed for these regions. Relative changes in summer sea-ice reach up to -100 % in the northern Barent- and north east Greenland Sea. This area is already reported as ice-free in the IPCC report in September, while it represents the peak area of decrease in sea-ice in March. This shows a good approximation of sea-ice trends in the AO compared to observational data. These findings correlate with the increase in simulated PAR (in summer months June to September) in areas of sea-ice decline in summer months (Fig. **22**C). Also, in this study, highest temperature increase correlates with highest sea-ice decline, which can be explained by the stronger increase of surface temperature due to higher absorption of energy from sunlight in ice-free, hence darker coloured regions.

Due to increased sea ice melt, also the MLD increased in the model by up to 2 meters per year around Svalbard and a slight decrease in the ice-free Norwegian Sea (yearly average). These findings are supported by another modeling study from Hordoir et al. [69], which report an increase of MLD around Svalbard and a decrease in the Norwegian Sea (especially from winter to spring). In this paper, the cause of increasing MLD was identified to be the reduced haline stratification due to sea-ice melt (source of freshwater, hence reduction of salinity). This is also represented in this study, where

in regions of highest ice-melt, the MLD increases the most. Another reason for strong warming and sea-ice melt is the inflow of warm water from the Atlantic into the Eurasian Basin of the AO [70]. This is causing increased sea-ice melt, reduced stratification and increased vertical mixing, resulting in a deeper MLD.

4.3.2 Shifts in Phytoplankton Community over the past five Decades

The previously described environmental changes also drive changes in the phytoplankton community in the AO. While in the global ocean there is a negative trend of total NPP by - 6.52 % (Fig. **16**/2A), a positive trend of + 22.98 % can be observed in the AO (Fig. **16**/2B). Furthermore, phaeocystis NPP increases by 36.06 % in the AO (Fig. **16**/1B). To allocate these trends in NPP to regions in the AO, figures 17 to 20 show changes in NPP and Chl-a both, total and for the four pPFTs separately, in an AO map. All of them show a decrease of total NPP in the central AO, as well as in the northern Baffin Bay, the Norwegian Sea and along the coast of east Russia. These decreases are likely due to the strong decrease of diatom NPP, which cannot be compensated by the increase of NPP of other pPFTs.

In the region around Svalbard, the trends created in this study show increased total Chl-a and NPP of pPFTs. Relative trends (Fig. **18** – NPP; Fig. **20** – Chl-a) reveal an increase of all four pPFTs. This can be explained by the increase in light and temperature which increases PP of the pPFTs [30]. Among the increasing pPFTs, haptophyte pPFTs phaeocystis and coccolithophores are increasing along the inflow current from the Atlantic Ocean (so-called Atlantification of the AO), which was hypothesized in this study and also reproduces results from Oziel et al. [71], Orkney et al. [37] and Nöthig et al. [38]. While the time series of NPP of small phytoplankton, coccolithophores and phaeocystis in the AO show a increasing relative trend of 97.68 %, 64.24 % and 36.06 %, respectively (Appendix .2), the diatom NPP increases only by 1.78 %. A reason for this could be the decrease in DSi in the AO, which negative trend is shown in figure **22**E. When comparing the relative trend of diatom NPP and Chl-a to the relative trend of DSi, a correlation in the pattern can be observed. While diatoms decrease in the central AO, East Siberian Sea, Laptev Sea and Baffin Bay and Hudson Bay, DSi shows decreasing hotspots in the East Siberian Sea, the Baffin Bay as well as the Hudson Bay. In the region around Svalbard, where diatoms are also increasing, DSi is decreasing only slightly. This finding supports the hypothesis that diatoms are decreasing in the AO due to decreasing DSi in the AO. Therefore, DSi is becoming increasingly the limiting factor of diatom growth. The reason for decreasing silicate in the AO is the poleward transportation of Atlantic waters, which is poor in DSi [35]. This however, raises the question why diatoms are still increasing in the north-east Green-

land Sea and western Barent Sea, an area which is also affected by decreased DSi concentrations [35]. A reason for this might be that DSi concentrations are still sufficient for the increase in diatom NPP observed; however, this region might also become DSi limited in the future and thereby limiting the growth of diatoms in the future, also in this region. This will then favor the current shift, seen in the phytoplankton community in the AO even more. However, this would require further investigation of limiting factors in the AO of diatoms and the other pPFTs as well as future projections. Another study from Debyser et al. [72] found that riverine inputs of DSi and DIN in the Fram strait is increasing. This might compensate for the decreasing DSi input via Atlantic waters and would keep diatoms in the pPFT community in the Fram Strait.

As the other pPFTs do not rely on DSi, they might be able to outcompete diatoms in some regions, such as the central Arctic and the coastal areas of the AO. As they rely on DIN, an increasing nutrient supply (especially of DIN) in the AO can lead to an increase in their biomass. This nutrient increase is due to inflow of Pacific waters into the Chukchi Sea and Atlantic waters into the Eurasian Basin [17]. However, when looking at the trend of DIN (Fig. **22**D), it also shows a decreasing pattern, with relative trends up to -3.5 % in the East Siberian Sea (Appendix .3). This trend is largely due to the fact that increasing DIN can increase phytoplankton NPP (of small phytoplankton, coccolithophores and phaeocystis), due to higher light availability due to sea-ice melt (Fig. **22**B and C). So far, in the AO light was a main limiting factor. However, due to sea-ice melt, PAR is becoming less limited. Therefore, the combination of increased PAR and increased DIN causes increased phytoplankton NPP. In the relative trend of Arctic DIN concentration (Appendix .3), a strong decrease can be observed in the russian shelves, even though literature reports increasing DIN in these areas by inflow of Atlantic waters [30] [17] [71]). This lets suggest that the model misses sources of DIN close to east Russian shelves, likely due to underestimated riverine inflow or overestimated denitrification processes in these regions by the model.

4.3.3 Change in C-export Flux caused by Shift in Phytoplankton Community and Environmental Factors

To investigate if the increases in phytoplankton NPP also causes an increased C-export in the AO, also the C-export flux trends were analysed. A timeseries of the C-export flux in the global ocean shows a decreasing trend, which correlates with the decreasing total global NPP. However, when looking at the timeseries of the AO, the C-export flux keeps decreasing relatively by 7.45 %, even though the relative total NPP is increasing by 22.98 % (Fig. **16**/2B and 3B). On the one hand, this might suggest that the di-

atom NPP (relative increase only by 1.78 %) is largely responsible for the AO C-export flux. On the other hand, the timeseries of C-export flux only includes export fluxes at 100 m depth. As the AO has many areas with a lower depth (seen in the trend maps in figure **21**, marked as areas with 'no data') this might only indicate a shift of export towards more shallow coastal regions, and, hence, increasing export is not captured in the analysis when only looking at the 100 m depth horizon. To analyse the C-export flux at these shallower regions, trend maps of export flux at 30 m depth were plotted (Fig. **21**/2). When comparing the two export depths, it can be seen that more export is happening at a shallower depth, i.e. in the Chukchi Sea and in the north-east of the Greenland Sea, where the relative export increases stronger at 30 m depth than at 100 m depth. However, it is important to keep in mind that the export at 30 m depth does only include the remineralization up to this point. As in the upper ocean euphotic zone the remineralization is still higher than in the mesopelagic zone below 100 m, a higher remineralization can be expected between 30 and 100 m than below 100 m. This reduces C-export flux at increasing depths and makes it difficult to define the sinking POC flux at 30 m as "export". Therefore, the 30 m should only be considered in regions where the 100 m export flux cannot be analysed because they are shallower than 100 m.

Furthermore, an increase of NPP does not necessarily directly implicate a higher C-export. A study from Fadeev et al. [73] shows a decreased export in ice-free areas by *Phaeocystis spp.* compared to ice-covered, diatoms-dominating regions in the Fram Strait (west of Svalbard). This would agree with the timeseries showing C-export flux at 100 m depth decreasing in the AO and would support the hypothesis that this is due to a decrease of diatom NPP in the AO (Fig. **16**/3B; Appendix .2C). Another study from Rogge et al. [74] points out that the export of carbon in shallow AO waters depends on the outflow of these dense waters at the shallow ground to the deep ocean. Only then C will be exported and stored away from the atmosphere for longer periods of time.

4.3.4 Possible Role of *Phaeocystis spp.* in the BCP of the AO

This study shows that there is a shift in the phytoplankton community towards a lower contribution of diatoms and a higher contribution of small phytoplankton and haptophytes like coccolithophores and phaeocystis. Phaeocystis is increasing in the Eurasian Basin, but also is increasing towards the central AO (Fig. **17**E, most prominent where sea-ice melt is highest). Hence, a further melt in sea-ice and increase in PAR and DIN in the future, might cause an increased expansion of phaeocystis in the central AO. Also, especially because the AO is projected to become ice-free in summer in the second half of this century [24]. A study from 2017 already discovered a

bloom dominated by P. pouchetii underneath the ice towards the central AO [75]. The combined picture of the results from the present study and from observational studies suggests that *Phaeocystis* might also have an impact on the contribution to the BCP. My investigations show that while the export in the central AO decreased in the past decades, likely due to a decrease in diatom NPP in this region, the increase in phaeocystis NPP has the potential to compensate for this decrease in export. In the following this hypothesis will be discussed:

The C-export is dependent on many physical and environmental factors. Among them are the MLD and biological community composition. As discussed earlier, the increased C-export in the region of the north-east of Greenland Sea and the Barent Sea (Fig. **21**/1) is likely due to increased NPP in combination with increased vertical mixing and the deeper MLD. In addition, an observational study shows that the warm water inflow from the Atlantic has caused a shift in the zooplankton community towards more macrozooplankton [76]. As these also graze on *Phaeocystis*, and also the degenerated foam after a bloom, *Phaeocystis* might be responsible for an increased C-export flux in the future AO. However, a study on *P. globosa* shows that even if macrozooplankton actively feeds on *Phaeocystis* colonies, it apparently prefers other prey, i.e. ciliates and dinoflagellates, if available [77]. This would contradict the hypothesis of an increased C-export by *Phaeocystis*. Beyond this, in this study, C-export was defined in the same way for phaeocystis compared to the other pPFTs. The aggregation rate is identical for all pPFTs and aggregates are defined to have two different sinking speeds (slow and fast sinking detritus). These sinking speeds are scaled depending on calcite or silicate in these aggregates. Observational studies show that calcite aggregates from coccolithophores have a higher sinking velocity than diatom aggregates containing silicate [78], which is represented in the model from this study. However, as phaeocystis does neither incorporate calcite nor silicate in their aggregates, sinking speeds in the model will be lower than those of coccolithophores or diatoms. Therefore, phaeocystis aggregates have more time to be remineralized on the way. This might be the reason for why there was no particulate relationship observed between increased phaeocystis alone together with increased C-export observed in this study. Therefore, further analysis but also better knowledge about the enigmatic *Phaeocystis spp.*, such as grazing and export habits are required.

For now, it can be concluded that phaeocystis increases in the pPFT community, together with other PFTs such as coccolithophores and small phytoplankton. Those might outcompete diatoms in some regions, likely due to increasing DSi limitation in the future AO. In addition, their growth will be promoted by increasing inflow of DIN. Furthermore, regions of high importance for possible increasing C-export could be identified, such as the

north-east of the Greenland Sea, the northern Barent Sea, as well as the Chukchi Sea. However, to conclude on how this shift in the phytoplankton community will affect the C-export, further modeling and observational studies on biological and biogeochemical interactions of *Phaeocystis spp.* in the AO are required.

4.4 Limitations of this Study

Even though the model represents environmental factors as well as their trends well, some limitations remain. The significance of these trends should be assessed to evaluate their robustness. Furthermore, the trends do only show the linear development, however break points or regime shifts, when a linear trend passes into a different trend, are not captured here. Also, comparisons with previous model versions and observational data need to be treated with care, as the model spin-up of 60 years is likely too short to bring the model in a real steady state. Therefore, longer spin-ups would provide more reliable results. Additionally, these longer spin-up runs can be used as a base for future projections. This would be of high interest to analyse the development of the AO's phytoplankton community and the resulting C-export. Furthermore, the C-export of phaeocystis should be further studied and included in the model in a more specific way for phaeocystis.

5 Conclusion and Outlook

Phaeocystis was implemented successfully into the biogeochemical model REcoM3, using a tuning strategy which reveals valuable knowledge about the role of parameters in the tuning process. This can help in future implementations to directly focus on impactful parameters related to the needs of a new study.

Furthermore, it shows the importance of representing phaeocystis in biogeochemical models as its abundance increases together with small phytoplankton and coccolithophores in the AO in the recent decades. The still dominating pPFT diatoms are becoming less prominent due to silicate limitations in the AO. Importantly, a decrease of NPP in the central AO was reported in this study, caused by a decrease of diatoms which could not be compensated by the increase of other pPFTs . However, this study as well as observational data showed an increase of *Phaeocystis* also towards the central AO.

Additionally, *Phaeocystis spp.* can protect themselves from grazers by the mucus produced when colonies are formed, giving them an advantage over other phytoplankton species. How this mucus is involved in the C-export remains to be investigated. Due to this unclarity as well as lack of understanding of the full grazing patterns, which affect the impact of phaeocystis on the BCP, one cannot conclude that increasing NPP of phaeocystis is coupled to increased C-export. This is still to be studied.

However, phaeocystis is of high importance in biogeochemical models as they play a key role in the future BCP of the AO by either increasing or decreasing C-export. This could be investigated by future projections using this model version, in combination with a longerspin-up runs.

Furthermost, as it was not only implemented in the AO but also in the SO, it would be of high interest to investigate the role of it and how it is contributing to the BCP there, too.

6 Appendix

.1 Subregions of Arctic Ocean.

Eight subregions of the Arctic Ocean and their naming. ("Map of the Arctic region and the eight subregions (the Central Arctic... — Download Scientific Diagram," 2019) [79].

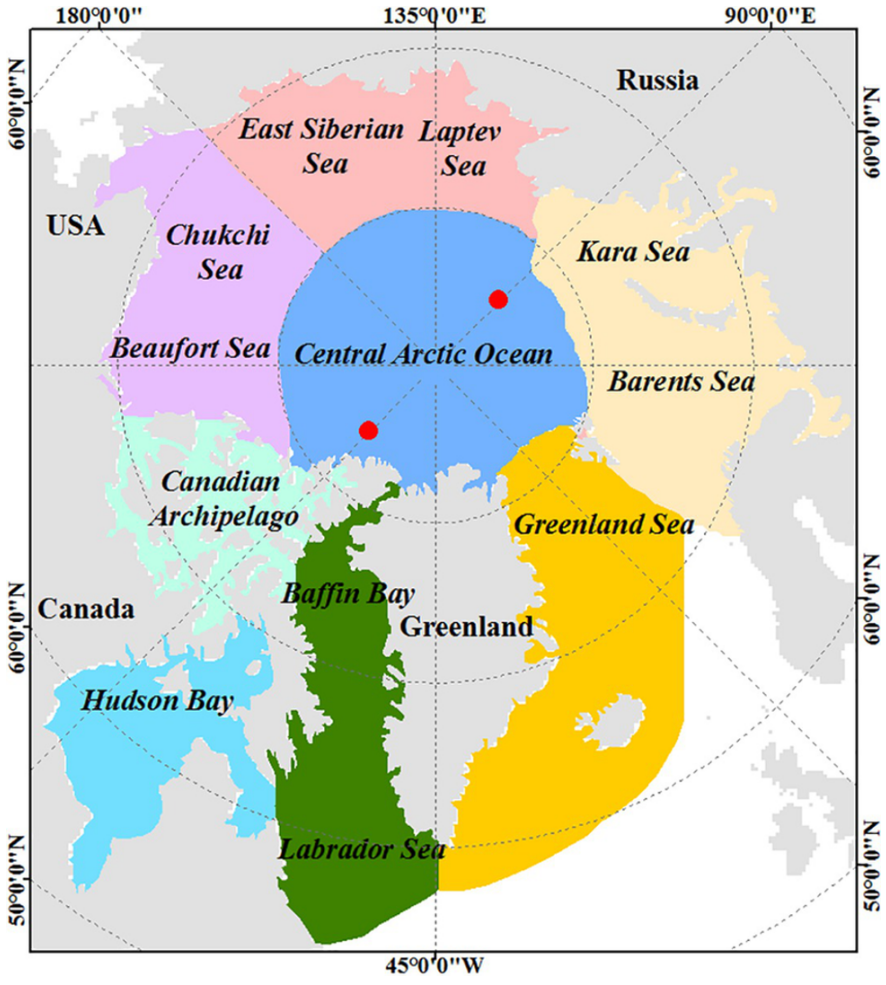

.2 NPP timeseries for the four pPFTs and total NPP in REcoM in the Arctic Ocean (AO) (1970-2023).

Model output data was averaged over the AO per year and is shown in blue, while a linear trend was calculated using the polyfit function from numpy and plotted in orange. The relative change between the first year (1970) and the last year (2023) was calculated and shown in the box. Note the different scales on the y-axis between the plots.

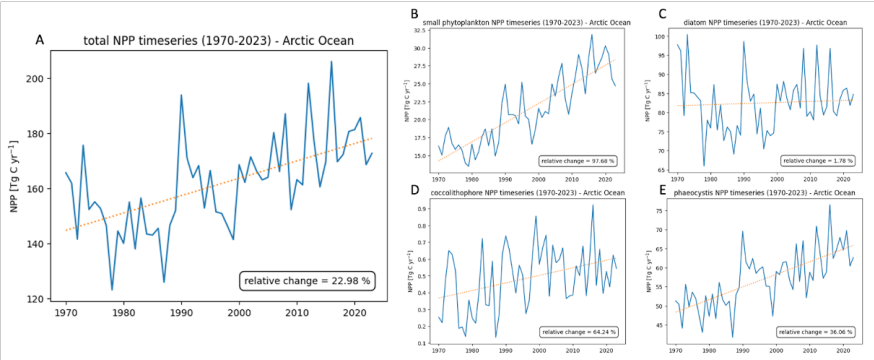

.3 Relative trends [% yr^{-1}] of environmental factors and nutrients in the AO (1970-2023).

Temperature (A), sea-ice coverage (SIC; B) and photosynthetically active radiation (PAR; C) are only plotted for the surface layer, while SIC and PAR only represent the trend of the summer months (Jun - Sep). Dissolved inorganic nitrogen (DIN; D) and dissolved inorganic silicate (DSi; E) are averaged over the upper 100 m. The mixed layer depth (MLD) is shown in F. All are calculated by taking the difference between the linear regression's first year and last year value and dividing it by the first year value multiplied by the years and finally multiplied by 100 %.

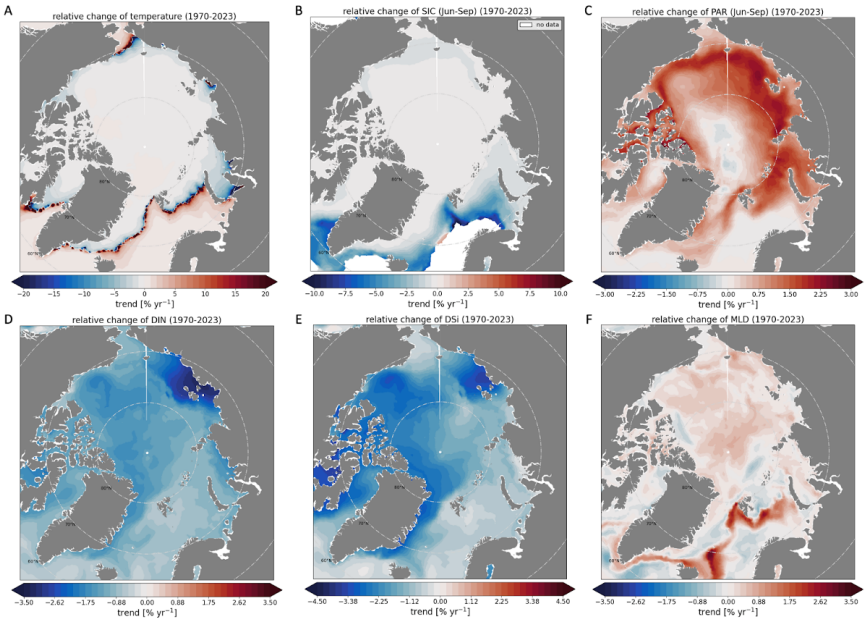

.4 List of software tools, versions and packages used in this study

Software	Version	Packages
Python	3.10.13	matplotlib, netCDF4, numpy, pandas, Cartopy, nbconvert, jupyter, scipy, scikit-learn, xarray, math, pathlib
R	4.4.1	readxl, minpack.lm, graphics, stats, utils, tidyr, magick, datasets, methods
Fortran	2021.6.0	-
Intel OpenAPI compiler	2022.1.0	-

Bibliography

[1] M. Consalvey, R. Perkins, D. Paterson, and G. Underwood. PAM fluorescence: A beginners guide for benthic diatomists. *Diatom Research*, 20:1–22, 2005.

[2] R.J. Geider, H.L. Maclntyre, and T.M. Kana. A dynamic regulatory model of phytoplanktonic acclimation to light, nutrients, and temperature. *Limnol. Oceanogr*, 43:679–694, 1998.

[3] M. Seifert, C. Nissen, B. Rost, and J. Hauck. Cascading effects augment the direct impact of CO2 on phytoplankton growth in a biogeochemical model. *Elementa: Science of the Anthropocene*, 10:00104, 2022.

[4] S.I. Anderson, A.D. Barton, S. Clayton, S. Dutkiewicz, and T.A. Rynearson. Marine phytoplankton functional types exhibit diverse responses to thermal change. *Nat. Commun*, 12:6413, 2021.

[5] S. Arrhenius. Über die Reaktionsgeschwindigkeit bei der Inversion von Rohrzucker durch Säuren. *Z. Für Phys. Chem*, 4U:226–248, 1889.

[6] V. Schoemann, S. Becquevort, J. Stefels, V. Rousseau, and C. Lancelot. Phaeocystis blooms in the global ocean and their controlling mechanisms: A review. *J. Sea Res., Iron Resources and Oceanic Nutrients - Advancement of Global Environmental Simulations*, 53:43–66, 2005.

[7] X. Wang, K. Tang, Y. Wang, and W. Smith. Temperature effects on growth, colony development and carbon partitioning in three Phaeocystis species. *Aquat. Biol*, 9:239–249, 2010.

[8] Buschmann. Labreport: Assessing thermal responses of arctic key phytoplankton species. Master's thesis, University of Bremen, 2022.

[9] H.E. Garcia, K.W. Weathers, C.R. Paver, I. Smolyar, T.P. Boyer, R.A. Locarnini, M.M. Zweng, A.V. Mishonov, O.K. Baranova, D. Seidov, and J.R. Reagan. Dissolved inorganic nutrients (phosphate, nitrate, silicate). Technical report, World ocean atlas 2018, 2019.

[10] J.-B. Sallée, V. Pellichero, C. Akhoudas, E. Pauthenet, L. Vignes, S. Schmidtko, A.N. Garabato, P. Sutherland, and M. Kuusela. Summertime increases in upper-ocean stratification and mixed-layer depth. *Nature*, 591:592–598, 2021.

[11] W. N. Meier, F. Fetterer, A. K. Windnagel, and J. S. Stewart. Noaa/nsidc climate data record of passive microwave sea ice concentration. (g02202, version 4). [data set]. Technical report, National Snow and Ice Data Center Boulder, Colorado USA., 2022.

[12] H.E. Garcia, R.A. Locarnini, T.P.| Boyer, J.I. Antonov, O.K. Baranova, M.M. Zweng, J.R. Reagan, D.R. Johnson, A.V. Mishonov, and S. Levitus. Dissolved inorganic nutrients (phosphate, nitrate, silicate). Technical report, World ocean atlas, 2013.

[13] R. Johnson, P.G. Strutton, S.W. Wright, A. McMinn, and K.M. Meiners. Three improved satellite chlorophyll algorithms for the Southern Ocean. *Journal of Geophysical Research: Oceans*, 118:3694–3703, 2013.

[14] S. Sathyendranath, R.J.W. Brewin, C. Brockmann, V. Brotas, B. Calton, A. Chuprin, P. Cipollini, A.B. Couto, J. Dingle, R. Doerffer, C. Donlon, M. Dowell, A. Farman, M. Grant, S. Groom, A. Horseman, T. Jackson, H. Krasemann, S. Lavender, V. Martinez-Vicente, C. Mazeran, F. Mélin, T.S. Moore, D. Müller, P. Regner, S. Roy, C.J. Steele, F. Steinmetz, J. Swinton, M. Taberner, A. Thompson, A. Valente, M. Zühlke, V.E. Brando, H. Feng, G. Feldman, B.A. Franz, R. Frouin, R.W. Gould, S.B. Hooker, M. Kahru, S. Kratzer, B.G. Mitchell, F.E. Muller-Karger, H.M. Sosik, K.J. Voss, J. Werdell, and T. Platt. An ocean-colour time series for use in climate studies: The experience of the ocean-colour climate change initiative (OC-CCI. *Sensors*, 19:4285, 2019.

[15] T. Westberry, M. J. Behrenfeld, D. A. Siegel, and E. Boss. Carbon-based primary productivity modeling with vertically resolved photoacclimation., 2008.

[16] M.J. Behrenfeld and P.G. Falkowski. A consumer's guide to phytoplankton primary productivity models, 0.

[17] K.M. Lewis, G.L. Dijken, and K.R. Arrigo. Changes in phytoplankton concentration now drive increased Arctic Ocean primary production. *Science*, 369:198–202, 2020.

[18] P. Friedlingstein, M. O'Sullivan, M.W. Jones, R.M. Andrew, D.C.E. Bakker, J. Hauck, P. Landschützer, C. Le Quéré, I.T. Luijkx, G.P. Peters, W. Peters, J. Pongratz, C. Schwingshackl, S. Sitch, J.G. Canadell, P. Ciais, R.B. Jackson, S.R. Alin, P. Anthoni, L. Barbero, N.R. Bates, M. Becker, N. Bellouin, B. Decharme, L. Bopp, I.B.M. Brasika, P. Cadule, M.A. Chamberlain, N. Chandra, T.-T.-T. Chau, F. Chevallier, L.P. Chini, M. Cronin, X. Dou, K. Enyo, W. Evans, S. Falk, R.A. Feely, L. Feng, D.J. Ford, T. Gasser, J. Ghattas, T. Gkritzalis, G. Grassi, L. Gregor, N. Gruber, Ö. Gürses, I. Harris, M. Hefner, J. Heinke, R.A. Houghton, G.C. Hurtt, Y. Iida, T. Ilyina, A.R. Jacobson, A. Jain, T. Jarníková, A. Jersild, F. Jiang, Z. Jin, F. Joos, E. Kato, R.F. Keeling, D. Kennedy, K. Klein Goldewijk, J. Knauer, J.I. Korsbakken,

A. Körtzinger, X. Lan, N. Lefèvre, H. Li, J. Liu, Z. Liu, L. Ma, G. Marland, N. Mayot, P.C. McGuire, G.A. McKinley, G. Meyer, E.J. Morgan, D.R. Munro, S.-I. Nakaoka, Y. Niwa, K.M. O'Brien, A. Olsen, A.M. Omar, T. Ono, M. Paulsen, D. Pierrot, K. Pocock, B. Poulter, C.M. Powis, G. Rehder, L. Resplandy, E. Robertson, C. Rödenbeck, T.M. Rosan, J. Schwinger, R. Séférian, T.L. Smallman, S.M. Smith, R. Sospedra-Alfonso, Q. Sun, A.J. Sutton, C. Sweeney, S. Takao, P.P. Tans, H. Tian, B. Tilbrook, H. Tsujino, F. Tubiello, and B. Global carbon budget 2023. *Earth System Science Data*, 15:5301–5369, 2023.

[19] E. Maier-Reimer, U. Mikolajewicz, and A. Winguth. Future ocean uptake of CO2: Interaction between ocean circulation and biology, 1996.

[20] T. Volk and M.I. Hoffert. Ocean carbon pumps: Analysis of relative strengths and efficiencies in ocean-driven atmospheric CO2 changes. *The Carbon Cycle and Atmospheric CO 2 : Natural Variations Archean to Present. Chapman Conference Papers*, 32:99–110, 1985.

[21] P.W. Boyd, H. Claustre, M. Levy, D.A. Siegel, and T. Weber. Multifaceted particle pumps drive carbon sequestration in the ocean. *Nature*, 568:327–335, 2019.

[22] M.H. Iversen. Carbon export in the ocean: A biologist's perspective. *Annual Review of Marine Science*, 15:357–381, 2023.

[23] D.A. Siegel, T. DeVries, I. Cetinić, and K.M. Bisson. Quantifying the ocean's biological pump and its carbon cycle impacts on global scales. *Annual Review of Marine Science*, 15:329–356, 2023.

[24] V. Masson-Delmotte. *Climate change 2021: the physical science basis: Working Group I contribution to the Sixth Assessment Report of the Intergovernmental Panel on Climate Change*. Cambridge University Press, Cambridge, 2023.

[25] K. Fennel, J.P. Mattern, S.C. Doney, L. Bopp, A.M. Moore, B. Wang, and L. Yu. Ocean biogeochemical modelling. *Nature Reviews Methods Primers*, 2(1):76, 2022.

[26] M. Meredith, M. Sommerkorn, S. Cassotta, C. Derksen, A. Ekaykin, A. Hollowed, G. Kofinas, A. Mackintosh, J. Melbourne-Thomas, M.M.C. Muelbert, G. Ottersen, H. Pritchard, and E.a G. Schuur. Polar regions. chapter 3, ipcc special report on the ocean and cryosphere in a changing climate. Technical report, Intergovernmental Panel On Climate Change (IPCC), 2023.

[27] M. Rantanen, A. Karpechko, A. Lipponen, K. Nordling, O. Hyvarinen, K. Ruosteenoja, T. Vihma, and A. Laaksonen. The arctic has warmed

nearly four times faster than the globe since 1979. *Communications Earth and Environment*, 3:168, 08 2022.

[28] Q Shu, Q Wang, M. Årthun, S. Wang, Z Song, M Zhang, and F. Qiao. Arctic ocean amplification in a warming climate in cmip6 models. *Science Advances*, 8(30):eabn9755, 2022.

[29] X. Wang, Y. Liu, J.R. Key, and R. Dworak. A new perspective on four decades of changes in arctic sea ice from satellite observations. *Remote Sens*, 14:1846, 2022.

[30] K. Arrigo and G. Dijken. Continued increases in Arctic Ocean primary production. *Prog. Oceanogr*, 136, 2015.

[31] M. Nowicki, T. DeVries, and D.A. Siegel. Quantifying the carbon export and sequestration pathways of the ocean's biological carbon pump. *Global Biogeochemical Cycles*, 36:2021 007083, 2022.

[32] D.K. Steinberg and M.R. Landry. Zooplankton and the ocean carbon cycle. *Annual Review of Marine Science*, 9:413–444, 2017.

[33] A. Tagliabue, L. Kwiatkowski, L. Bopp, M. Butenschön, W. Cheung, M. Lengaigne, and J. Vialard. Persistent uncertainties in ocean net primary production climate change projections at regional scales raise challenges for assessing impacts on ecosystem services. *Front. Clim*, 3, 2021.

[34] S. A. Henson, C. Laufkötter, S. Leung, S. L. C. Giering, H. I. Palevsky, and E. L. Cavan. Uncertain response of ocean biological carbon export in a changing world. *Nature Geoscience*, 15(4):248–254, 2022.

[35] H. Hátún, K. Azetsu-Scott, R. Somavilla, F. Rey, C. Johnson, M. Mathis, U. Mikolajewicz, P. Coupel, J.-É. Tremblay, S. Hartman, S.V. Pacariz, I. Salter, and J. Ólafsson. The subpolar gyre regulates silicate concentrations in the North Atlantic. *Sci. Rep*, 7:14576, 2017.

[36] L. Oziel, A. Baudena, M. Ardyna, P. Massicotte, A. Randelhoff, J. Sallée, R. Ingvaldsen, E. Devred, and M. Babin. Faster Atlantic currents drive poleward expansion of temperate phytoplankton in the Arctic Ocean. *Nat. Commun*, 11, 2020.

[37] A. Orkney, T. Platt, B.E. Narayanaswamy, I. Kostakis, and H.A. Bouman. Bio-optical evidence for increasing phaeocystis dominance in the barents sea. *Phil. Trans. R. Soc. A.*, 378:20190357, 2020.

[38] E.-M. Nöthig, E. Bauerfeind, K. Metfies, S. Simon, and C. Lorenzen. Chlorophyll a measured on water bottle samples during POLARSTERN cruise ARK-XXIV/2. *Polar research*, 2015.

[39] W.O. Smith and S. Trimborn. Phaeocystis: a global enigma. *Annual Review of Marine Science*, 16:417–441, 2024.

[40] L. B. Tremblay, G. A. Schmidt, S. Pfirman, R. Newton, and P. DeRepentigny. Is ice-rafted sediment in a north pole marine record evidence for perennial sea-ice cover? *Philosophical Transactions of the Royal Society A*, 373(2052), 2015.

[41] P. Bradley, M. Sanderson, J. Nejstgaard, A. Sazhin, M. Frischer, L. Killberg-Thoreson, P. Verity, L. Campbell, and D. Bronk. Nitrogen uptake by phytoplankton and bacteria during an induced Phaeocystis pouchetii bloom, measured using size fractionation and flow cytometric sorting. *Aquatic Microbial Ecology*, 61:89–104, 2010.

[42] Ö. Gürses, L. Oziel, O. Karakuş, D. Sidorenko, C. Völker, Y. Ye, M. Zeising, M. Butzin, and J. Hauck. Ocean biogeochemistry in the coupled ocean–sea ice–biogeochemistry model FESOM2.1–REcoM3. *Geosci. Model Dev*, 16:4883–4936, 2023.

[43] S. Danilov, D. Sidorenko, Q. Wang, and T. Jung. The finite-volumE sea ice–Ocean model (FESOM2. *Geoscientific model development*, 10:765–789, 2017.

[44] Python Software Foundation. Python: Version 3.10.13. `https://www.python.org/`, 2023. Software.

[45] R Core Team. R: A language and environment for statistical computing. `https://www.R-project.org/`, 2024. Software, Vienna: R Foundation for Statistical Computing.

[46] O. Karakuş, C. Völker, M. Iversen, W. Hagen, D. Wolf-Gladrow, B. Fach, and J. Hauck. Modeling the impact of macrozooplankton on carbon export production in the southern ocean. *Journal of Geophysical Research: Oceans*, 126:2021 017315, 2021.

[47] J.A. Cram, T. Weber, S.W. Leung, A.M.P. McDonnell, J.-H. Liang, and C. Deutsch. The role of particle size, ballast, temperature, and oxygen in the sinking flux to the deep sea. *Global Biogeochemical Cycles*, 32:858–876, 2018.

[48] O. Karakuş, C. Völker, M. Iversen, W. Hagen, and J. Hauck. The role of zooplankton grazing and nutrient recycling for global ocean biogeochemistry and phytoplankton phenology. *Journal of Geophysical Research: Biogeosciences*, 127:2022 006798, 2022.

[49] H. Tsujino, S. Urakawa, H. Nakano, R.J. Small, W.M. Kim, S.G. Yeager, G. Danabasoglu, T. Suzuki, J.L. Bamber, M. Bentsen, C.W.

Böning, A. Bozec, E.P. Chassignet, E. Curchitser, F. Boeira Dias, P.J. Durack, S.M. Griffies, Y. Harada, M. Ilicak, S.A. Josey, C. Kobayashi, S. Kobayashi, Y. Komuro, W.G. Large, J. Le Sommer, S.J. Marsland, S. Masina, M. Scheinert, H. Tomita, M. Valdivieso, and D. Yamazaki. JRA-55 based surface dataset for driving ocean–sea-ice models (JRA55-do. *Ocean Modelling*, 130:79–139, 2018.

[50] O. Aumont, J.C. Orr, P. Monfray, G. Madec, and E. Maier-Reimer. Nutrient trapping in the equatorial Pacific: The ocean circulation solution. *Global Biogeochemical Cycles*, 13:351–369, 1999.

[51] P. Scholz, D. Sidorenko, O. Gurses, S. Danilov, N. Koldunov, Q. Wang, D. Sein, M. Smolentseva, N. Rakowsky, and T. Jung. Assessment of the Finite-volumE Sea ice-Ocean Model (FESOM2.0) – Part 1: Description of selected key model elements and comparison to its predecessor version. *Geosci. Model Dev*, 12:4875–4899, 2019.

[52] S. Danilov, Q. Wang, R. Timmermann, N. Iakovlev, D. Sidorenko, M. Kimmritz, T. Jung, and J. Schröter. Finite-element sea ice model (FESIM), version 2. *Geosci. Model Dev*, 8:1747–1761, 2015.

[53] O. Karakuş. *The Role of Zooplankton for Carbon Export, Nutrient Recycling and Phytoplankton Bloom Phenology in an Ocean Biogeochemical Model*. PhD thesis, University of Bremen, 2022.

[54] L.T. Bach. Reconsidering the role of carbonate ion concentration in calcification by marine organisms. *Biogeosciences (Online)*, 12:4939–4951, 2015.

[55] E. Álvarez, S. Thoms, and C. Völker. Chlorophyll to Carbon Ratio Derived From a Global Ecosystem Model With Photodamage. *Global Biogeochemical Cycles*, 32(5):799–816, 2018.

[56] G.M. Grimaud, F. Mairet, A. Sciandra, and O. Bernard. Modeling the temperature effect on the specific growth rate of phytoplankton: A review. *Rev Environ Sci Biotechnol*, 16:625–645, 2017.

[57] D. C. López-Sandoval, T. Rodríguez-Ramos, P. Cermeño, C. Sobrino, and E. Marañón. Photosynthesis and respiration in marine phytoplankton: Relationship with cell size, taxonomic affiliation, and growth phase. *Journal of Experimental Marine Biology and Ecology*, 457:151–159, 2014.

[58] D. Bozzato, T. Jakob, and C. Wilhelm. Effects of temperature and salinity on respiratory losses and the ratio of photosynthesis to respiration in representative Antarctic phytoplankton species. *PLOS ONE*, 14:0224101, 2019.

[59] M. Vogt, C. O'Brien, J. Peloquin, V. Schoemann, E. Breton, M. Estrada, J. Gibson, D. Karentz, M.A. Leeuwe, J. Stefels, C. Widdicombe, and L. Peperzak. Global marine plankton functional type biomass distributions: Phaeocystis spp. *Earth System Science Data*, 4:107–120, 2012.

[60] K.M. Lewis and K.R. Arrigo. Ocean color algorithms for estimating chlorophyll a, CDOM absorption, and particle backscattering in the arctic ocean. *Journal of Geophysical Research: Oceans*, 125:2019 015706, 2020.

[61] J. Marra, C. Langdon, and C.A. Knudson. Primary production, water column changes, and the demise of a Phaeocystis bloom at the Marine Light-Mixed Layers site (59°N, 21°W) in the northeast Atlantic Ocean. *Journal of Geophysical Research: Oceans*, 100:6633–6643, 1995.

[62] P.G. Verity, T.J. Smayda, and E. Sakshaug. Photosynthesis, excretion, and growth rates of Phaeocystis colonies and solitary cells. *Polar research*, 10:117–128, 1991.

[63] H. Jakobsen and K. Tang. Effect of protozoan grazing on colony formation in Phaeocystis globosa (Prymnesiophyceae) and the potential costs and benefits. *Aquatic Microbial Ecology*, 27:261–273, 2002.

[64] C. Nissen and M. Vogt. Factors controlling the competition between Phaeocystis and diatoms in the Southern Ocean and implications for carbon export fluxes. *Biogeosciences (Online)*, 18:251–283, 2021.

[65] K.E. Taylor. Summarizing multiple aspects of model performance in a single diagram. *J. Geophys. Res. Atmospheres*, 106:7183–7192, 2001.

[66] C. Boyer Montégut, G. Madec, A.S. Fischer, A. Lazar, and D. Iudicone. Mixed layer depth over the global ocean: An examination of profile data and a profile-based climatology. *Journal of Geophysical Research: Oceans*, 109, 2004.

[67] A. E. West and E. W. Blockley. CMIP6 models overestimate sea ice melt, growth & conduction relative to ice mass balance buoy estimates, 2024.

[68] P.J. Tréguer, J.N. Sutton, M. Brzezinski, M.A. Charette, T. Devries, S. Dutkiewicz, C. Ehlert, J. Hawkings, A. Leynaert, S.M. Liu, N. Llopis Monferrer, M. López-Acosta, M. Maldonado, S. Rahman, L. Ran, and O. Rouxel. Reviews and syntheses: The biogeochemical cycle of silicon in the modern ocean. *Biogeosciences (Online)*, 18:1269–1289, 2021.

[69] R. Hordoir, Ø. Skagseth, R.B. Ingvaldsen, A.B. Sandø, U. Löptien, H. Dietze, A.M.U. Gierisch, K.M. Assmann, Ø. Lundesgaard, and S. Lind. Changes in arctic stratification and mixed layer depth cycle: A modeling analysis. *Journal of Geophysical Research: Oceans*, 127:2021 017270, 2022.

[70] I.V. Polyakov, A.V. Pnyushkov, M.B. Alkire, I.M. Ashik, T.M. Baumann, E.C. Carmack, I. Goszczko, J. Guthrie, V.V. Ivanov, T. Kanzow, R. Krishfield, R. Kwok, A. Sundfjord, J. Morison, R. Rember, and A. Yulin. Greater role for atlantic inflows on sea-ice loss in the eurasian basin of the arctic ocean. *Science*, 356:285–291, 2017.

[71] L. Oziel, G. Neukermans, M. Ardyna, C. Lancelot, J.-L. Tison, P. Wassmann, J. Sirven, D. Ruiz-Pino, and J.-C. Gascard. Role for Atlantic inflows and sea ice loss on shifting phytoplankton blooms in the Barents Sea. *Journal of Geophysical Research: Oceans*, 122:5121–5139, 2017.

[72] M.C.F. Debyser, L. Pichevin, R.E. Tuerena, P.A. Dodd, A. Doncila, and R.S. Ganeshram. Tracing the role of Arctic shelf processes in Si and N cycling and export through the Fram Strait: Insights from combined silicon and nitrate isotopes. *Biogeosciences (Online)*, 19:5499–5520, 2022.

[73] E. Fadeev, A. Rogge, S. Ramondenc, E.-M. Nöthig, C. Wekerle, C. Bienhold, I. Salter, A.M. Waite, L. Hehemann, A. Boetius, and M.H. Iversen. Sea ice presence is linked to higher carbon export and vertical microbial connectivity in the Eurasian Arctic Ocean. *Commun. Biol*, 4:1–13, 2021.

[74] A. Rogge, M. Janout, N. Loginova, E. Trudnowska, C. Hörstmann, C. Wekerle, L. Oziel, V. Schourup-Kristensen, E. Ruiz-Castillo, K. Schulz, V.V. Povazhnyy, M.H. Iversen, and A.M. Waite. Carbon dioxide sink in the Arctic Ocean from cross-shelf transport of dense Barents Sea water. *Nat. Geosci*, 16:82–88, 2023.

[75] P. Assmy, M. Fernández-Méndez, P. Duarte, A. Meyer, A. Randelhoff, C.J. Mundy, L.M. Olsen, H.M. Kauko, A. Bailey, M. Chierici, L. Cohen, A.P. Doulgeris, J.K. Ehn, A. Fransson, S. Gerland, H. Hop, S.R. Hudson, N. Hughes, P. Itkin, G. Johnsen, J.A. King, B.P. Koch, Z. Koenig, S. Kwasniewski, S.R. Laney, M. Nicolaus, A.K. Pavlov, C.M. Polashenski, C. Provost, A. Rösel, M. Sandbu, G. Spreen, L.H. Smedsrud, A. Sundfjord, T. Taskjelle, A. Tatarek, J. Wiktor, P.M. Wagner, A. Wold, H. Steen, and M.A. Granskog. Leads in Arctic pack ice enable early phytoplankton blooms below snow-covered sea ice. *Sci. Rep*, 7:40850, 2017.

[76] S. Ramondenc, E.-M. Nöthig, L. Hufnagel, E. Bauerfeind, K. Busch, N. Knüppel, A. Kraft, F. Schröter, M. Seifert, and M.H. Iversen. Effects of Atlantification and changing sea-ice dynamics on zooplankton community structure and carbon flux between 2000 and 2016 in the eastern Fram Strait. *Limnol. Oceanogr*, 68:39–53, 2023.

[77] K.W. Tang, H.H. Jakobsen, and A.W. Visser. Phaeocystis globosa (Prymnesiophyceae) and the planktonic food web: Feeding, growth, and trophic interactions among grazers. *Limnol. Oceanogr*, 46:1860–1870, 2001.

[78] M.H. Iversen and H. Ploug. Ballast minerals and the sinking carbon flux in the ocean: Carbon-specific respiration rates and sinking velocities of macroscopic organic aggregates (marine snow, 2010.

[79] Map of the arctic region and the eight subregions (the central arctic. In | *Download Scientific Diagram [WWW Document], n.d. URL.*

Statement of Independence

I hereby declare that I have written this thesis entirely on my own, without any unauthorized assistance, and that all sources used have been properly cited. Any parts of the work that are not my own are clearly marked with appropriate references. I further declare that this work has not been submitted elsewhere for evaluation, and I have not used any prohibited resources in the preparation of this work.

Date: December 16, 2024 **Signature:**